

CELL BIOLOGY

Cluster nanoarchitecture and structural diversity of PIEZO1 at rest and during activation in intact cells

Clement Verkest¹, Lucas Roettger¹, Nadja Zeitzschel¹, James Hall², Oscar Sánchez-Carranza², Angela Tzu-Lun Huang², Gary R. Lewin^{2,3,4}, Stefan G. Lechner^{1*}

The force-gated ion channel PIEZO1 confers mechanosensitivity to many cell types. While the structure and physiological roles of PIEZO1 are well-described, the subcellular distribution and the impact of the cellular microenvironment on PIEZO1 conformation and function are poorly understood. Here, using MINFLUX nanoscopy, we demonstrate that PIEZO1 channels accumulate in pit-shaped invaginations that are distinct from classical membrane invaginations such as clathrin-coated pits and caveolae, thereby possibly creating hotspots for mechanotransduction. Moreover, by measuring intramolecular distances in individual PIEZO1 channels with nanometer precision, we reveal subcellular compartment-specific differences in PIEZO1 conformation at rest and during activation that correlate with differences in PIEZO1 function and are possibly caused by differences in cytoskeletal architecture. Together, our data provide previously unrecognized insights into the complex interplay of forces that determine how PIEZO1 alters membrane shape and, vice versa, how the membrane together with the cytoskeleton affect the conformation and function of individual PIEZO1 channels.

INTRODUCTION

PIEZO1 is a mechanosensitive ion channel that enables a variety of cell types to detect and respond to mechanical stimuli and is thus essential for numerous physiological processes (1–5). With regard to PIEZO1 structure and function, cryo-electron microscopy (cryo-EM) studies together with high-speed atomic force microscopy (AFM) and in silico modeling have established a mechanistic framework, which proposes that PIEZO1 forms a propeller-shaped homotrimer that assumes a curved conformation at rest and transitions—via a partially flattened and intermediate open state—into a fully flattened conformation (6–17) upon activation. In the flattened state, the channel can be “open” or “inactivated,” depending on whether the cap-gated is closed or not (14).

This framework, however, rests on investigations of individual channels in artificial membranes and simplified model systems and thus has several limitations. First, in cryo-EM liposomes, PIEZO1 adopts different conformations depending on its orientation: Thus, in concave environments (i.e., when reconstituted in the inside-out orientation), PIEZO1 assumes a curved conformation (15–17), whereas it assumes the flattened conformation when reconstituted in the outside-out orientation (Fig. 1A) (7). Cryo-EM liposomes are, however, highly curved and only slightly bigger than PIEZO1 itself such that the channel is exposed to abnormally high bending forces when reconstituted in such liposomes, which raises the question whether the conformational states resolved by cryo-EM also exist in the native environment of the plasma membrane where such high degrees of membrane curvature are not observed. Second, in living cells, the membrane and possibly the channel itself, are tightly attached to the subjacent cytoskeleton, which is known to control PIEZO1 sensitivity (18–22). Yet, it is unclear whether and to what

extent the cytoskeleton alters PIEZO1 conformation and changes thereof upon mechanical activation. Mulhall *et al.* (23) recently reported that PIEZO1 appears to be more expanded in living cells than predicted by cryo-EM, indicating that the channel behaves differently in its native environment, although the cell intrinsic factors causing the observed partial flattening remained elusive.

Last, although it is well-established that individual PIEZO1 channels can function as independent mechanosensors (24, 25), PIEZO1 was shown to form prominent clusters in many cell types, both at endogenous expression levels and when recombinantly expressed in heterologous systems (20, 26–34). Using immunohistochemistry and genetic fluorophore tagging of PIEZO1, prominent cluster formation at endogenous expression levels was observed in rodent and human tissues including keratinocytes (33, 34), endothelial cells (34), neural stem cells (34), dermal fibroblasts (35), glioblastoma stem cells (26), microglia (29), cardiomyocytes (32), and trigeminal ganglia (31). PIEZO1 does not appear to form clusters in red blood cells, as suggested by stimulated emission depletion superresolution microscopy (36), although conflicting results were obtained using force distance-based AFM (37). Regarding the functional relevance of PIEZO1 clusters, two elegant studies in which calcium sensors were fused to the C terminus of PIEZO1, demonstrated that clusters mediate calcium influx in response to mechanical and chemical activation of PIEZO1 (34, 38). Moreover, in some cell types, PIEZO1 clusters are recruited to hot spots of mechanotransduction such as focal adhesions (26, 28, 30), the rear edge of migrating keratinocytes (33) and t-tubules in cardiomyocytes (32), which further supports an important role of PIEZO1 clusters in cellular mechanosensitivity. In the curved conformation, PIEZO1 locally deforms the membrane into a dome shape that extends far beyond the perimeter of the channel such that the membrane footprint of PIEZO1 is much bigger than the channel itself (15–17), which supposedly has important implications regarding the impact of clustering on PIEZO1 conformation and function. Thus, it has been proposed that the opposing curvatures of the membrane footprints of two nearby channels would create an energetic constraint in the interjacent membrane such that nearby channels would either repel each other or induce mutual flattening to reduce the overall energy

¹Department of Anaesthesiology, University Medical Center Hamburg-Eppendorf, Hamburg, Germany. ²Max Delbrück Center for Molecular Medicine in the Helmholtz Association (MDC), Molecular Physiology of Somatic Sensation Laboratory Berlin, Berlin, Germany. ³Charité-Universitätsmedizin Berlin, Berlin, Germany. ⁴German Center for Mental Health (DZPG), partner site Berlin, Berlin, Germany.

*Corresponding author. Email: s.lechner@uke.de

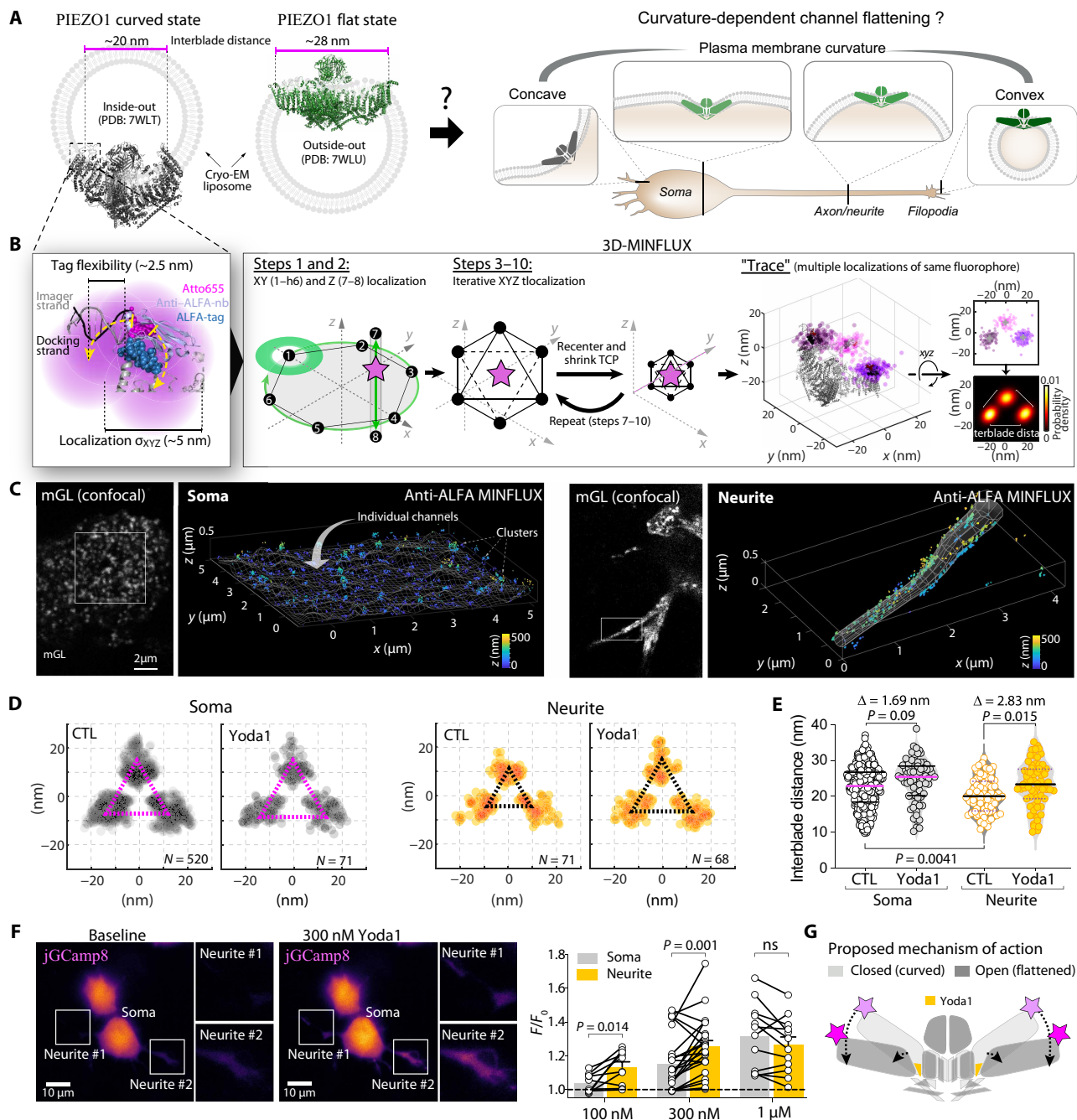


Fig. 1. 3D-MINFLUX reveals cell compartment-specific conformational heterogeneity of PIEZO1. (A) side views of curved (black) and flattened (green) PIEZO1 cryo-EM structures with interblade distance marked by purple lines (left) and cartoon depicting variations in membrane curvature in cellular compartments (right) (B) Close-up view of DNA-PAIN labeling system (left), schematic representation of MINFLUX imaging sequence (middle), and example of MINFLUX traces originating from a triple-labeled PIEZO1 trimer in 3D as well as 2D in-plane projection and probability density plot showing individual protomer localization. (C) Confocal images (left) of soma and highly curved neurite (right) showing PIEZO1-ALFA-mGL expression together with 3D views of the corresponding MINFLUX localization data (right) from the marked regions. (D) Overlays of trimers found in somata (black) or neurite (orange) generated by aligning the trace means of each identified trimer to a reference trimer. (E) Violin plots of interblade distances of trimers residing in somata (black) and neurites (orange) in the presence (open circles) and absence (filled circles) of Yoda1. Comparison with nonparametric Kruskal-Wallis analysis of variance (ANOVA) (P values are indicated in graph and N -numbers are the same as in (D)). (F) Fluorescence images with close-up views of neurites (left) of N2a-P1KO cells coexpressing PIEZO1-mScarlet and jGCaMP8m before and after the application of 300 nM Yoda1. Bar graph shows pairwise comparison of jGCaMP8 intensities (F/F_0) induced by the indicated concentrations of Yoda1 in somata (gray) and neurites (orange; paired t test. $N = 10$ (100 nM), $N = 23$ (300 nM), and $N = 12$ cells (1 μ M)). (G) Cartoon depicting the proposed binding site and mechanism of action of Yoda1 on PIEZO1. ns, not significant.

of the system (6, 12, 39). These hypotheses have, however, never been directly tested. Using two-dimensional (2D) stochastic optical reconstruction microscopy (STORM), Ridone and colleagues (27) demonstrated that PIEZO1 clusters are densely packed and contain multiple channels, but because of the lack of 3D information, the exact number of channels per cluster and their spatial arrangement remained elusive.

Here, we thus set out to examine the nanoarchitecture and the distribution of PIEZO1 within clusters as well as the possible role of other cell intrinsic factors in controlling PIEZO1 conformation at rest, using 3D-minimal fluorescence photon fluxes (MINFLUX) nanoscopy in combination with DNA-based point accumulation for imaging in nanoscale topography (DNA-PAINT) (40–42).

RESULTS

PIEZO1 conformation at rest differs between subcellular compartments

In proteoliposomes used for cryo-EM, PIEZO1 assumes a curved conformation with upward-tilted blades when reconstituted in the inside-out orientation (15–17), whereas it assumes a flattened conformation in which the distance between the distal ends of the blades is increased by ~8 nm (7) when reconstituted in the outside-out orientation (Fig. 1A). Accordingly, it has been proposed that membrane curvature governs PIEZO1 conformation, which raises the question as to whether cell compartment-specific differences in membrane curvature are sufficient to fine-tune PIEZO1 conformation and hence function at rest (Fig. 1A). To test this hypothesis, we measured the interblade distances (i.e., a surrogate measure for channel flattening; see Fig. 1A) of PIEZO1 trimers located at the flat soma-substrate interface and in neurites with highly curved membranes using MINFLUX nanoscopy in combination with DNA-PAINT, which achieves spatial resolutions in the nanometer range (Fig. 1B) (40–42). To this end, we expressed a PIEZO1 variant that carries an extracellular ALFA tag at the distal end of the blade domain and an mGreenLantern tag in the C terminus (PIEZO1-ALFA-mGL; fig. S1) in Neuro2a-PIEZO1 knock-out cells (43), labeled the ALFA tags with an anti-ALFA single domain nanobody conjugated to a DNA-PAINT docking strand, and imaged the cells with an Atto655-conjugated DNA-PAINT imager strand using 3D-MINFLUX (Fig. 1B and fig. S2 for negative controls and raw data processing).

To identify triple-labeled PIEZO1 trimers in MINFLUX localization data, we computed the Euclidian distance matrix of all localizations and searched for localization triplets in which the distances between the individual localizations were smaller than 40 nm (i.e., the maximal physically possible distance between two ALFA tags in the fully flattened state) and that had no other neighboring signals within 60 nm (see fig. S3, A and B as well as Materials and Methods for details on trimer identification rules). Using this algorithm, we identified 520 trimers in somata and 71 in neurites (Fig. 1, C to E; fig. S4A; and movies S1 and S2), with localization errors around 4 nm in xyz (fig. S3C). Note that because of the stringent trimer identification criteria, no trimers were detected in densely packed PIEZO1 clusters (Fig. 1C). To compare overall trimer geometries, we aligned the localization trace means of each trimer to a 2D reference trimer using an iterative closest point algorithm and overlaid the data. These overlays revealed elongated localization clouds extending outward from the trimer center, indicating that variability does not only result from the isotropic MINFLUX localization error (Fig. 1D) but

also reflects varying degrees of PIEZO1 flattening. Moreover, interblade angles (i.e., angles between the lines connecting the distal ends of the blades), while being uniformly distributed around 60°, showed notable variability (fig. S4B), indicating additional rotational flexibility of the distal blades, as previously reported (23).

Most notably, we found that the mean interblade distance was significantly smaller in neurites than in somata (neurite: 20.3 ± 4.9 nm; soma: 22.7 ± 5.6 nm; $P = 0.0041$, Kruskal-Wallis test; Fig. 1E), indicating that PIEZO1 is generally more contracted in neurites. Considering that PIEZO1 supposedly flattens during activation, we next examined the implications of the different degrees of PIEZO1 flattening in neurites and somata with regard to channel function. Assessing PIEZO1 mechanosensitivity in neurites is challenging because of limitations of standard patch-clamp techniques. In cell-attached pressure-clamp recordings, seal creep (44) induces F-actin reorganization (21), making this approach unsuitable for studying effects linked to cytoskeletal differences between neurites and soma. Whole-cell recordings also face issues, as space-clamp limitations prevent control of neurite membrane potential, precluding meaningful current comparisons. To overcome this, we used jGCaMP8 calcium imaging in intact cells to explore PIEZO1 sensitivity. Notably, neurites showed greater responses to 100 and 300 nM of the selective PIEZO1 activator Yoda1 compared to somata, although responses converged at higher concentrations (Fig. 1F). To rule out that the elevated calcium signals observed in neurites resulted from spatial confinement and limited Ca^{2+} diffusion in this small cell compartment, we compared GCaMP8 signals induced by increasing concentrations of Ca^{2+} in the presence of the ionophore ionomycin. In these experiments, Ca^{2+} signal intensities in neurites were even smaller than in somata (fig. S5, A to C), suggesting that the elevated calcium signals observed in response to Yoda1 indicate that PIEZO1 is more sensitive in neurites as compared to somata. Yoda1 is thought to activate PIEZO1 by acting as a molecular wedge that binds to a hydrophobic pocket at the proximal end of the blade domain, thereby promoting channel flattening (Fig. 1G) (45). We thus next asked whether the increased Yoda1 sensitivity in neurites corresponds to greater conformational changes in PIEZO1. Consistent with a prior report (23), we observed a subtle—yet nonsignificant—increase in the average interblade distance in the somata of cells fixed in the presence of Yoda1 (Δ 1.69 nm; CTL: 22.71 ± 5.68 nm, $N = 520$ versus Yoda1: 24.4 ± 6.01 nm, $N = 71$; $P = 0.095$, Kruskal-Wallis test; Fig. 1E). In neurites, by contrast, Yoda1 induced significant PIEZO1 flattening, increasing the mean interblade distance by 2.83 nm from 20.34 ± 4.88 nm (CTL, $N = 71$) to 23.17 ± 6.22 nm (Yoda1, $N = 68$, $P = 0.015$, Kruskal-Wallis test; Fig. 1E). Together our data show that PIEZO1 is more contracted in neurites as compared to somata and suggest that the channels conformation at rest affects its susceptibility to Yoda1-induced flattening, which appears to correlate with its chemosensitivity.

Local differences in cytoskeletal rigidity govern PIEZO1 conformation

The observation that PIEZO1 was more contracted in highly curved neurites as compared to the flat soma-substrate interface (Fig. 1) prompted us to explore the role of factors other than membrane curvature, which could differentially alter PIEZO1 conformation in neurites and somata. First—to corroborate our original observation—we examined the relationship between interblade distance and neurite diameter within the group of trimers detected in neurites, where

curvature varies, but other cell intrinsic factors likely do not. We did, however, not observe any correlation (Fig. 2A), suggesting that membrane curvature—at least at the microscale—only plays a minor role in controlling PIEZO1 conformation.

Another possible explanation for the observed differences in interblade distances comes from modeling studies, which have proposed that crowding of PIEZO1 may induce mutual flattening of

adjacent channels (39). However, there was no correlation between local channel density—i.e., average distances to the three nearest neighboring channels of the detected trimers—and the interblade distance within the two groups (Fig. 2B), indicating that differences in crowding do not contribute to the observed differences in interblade distances. This statement only holds true for channels that are located outside of densely packed PIEZO1 clusters because our strict

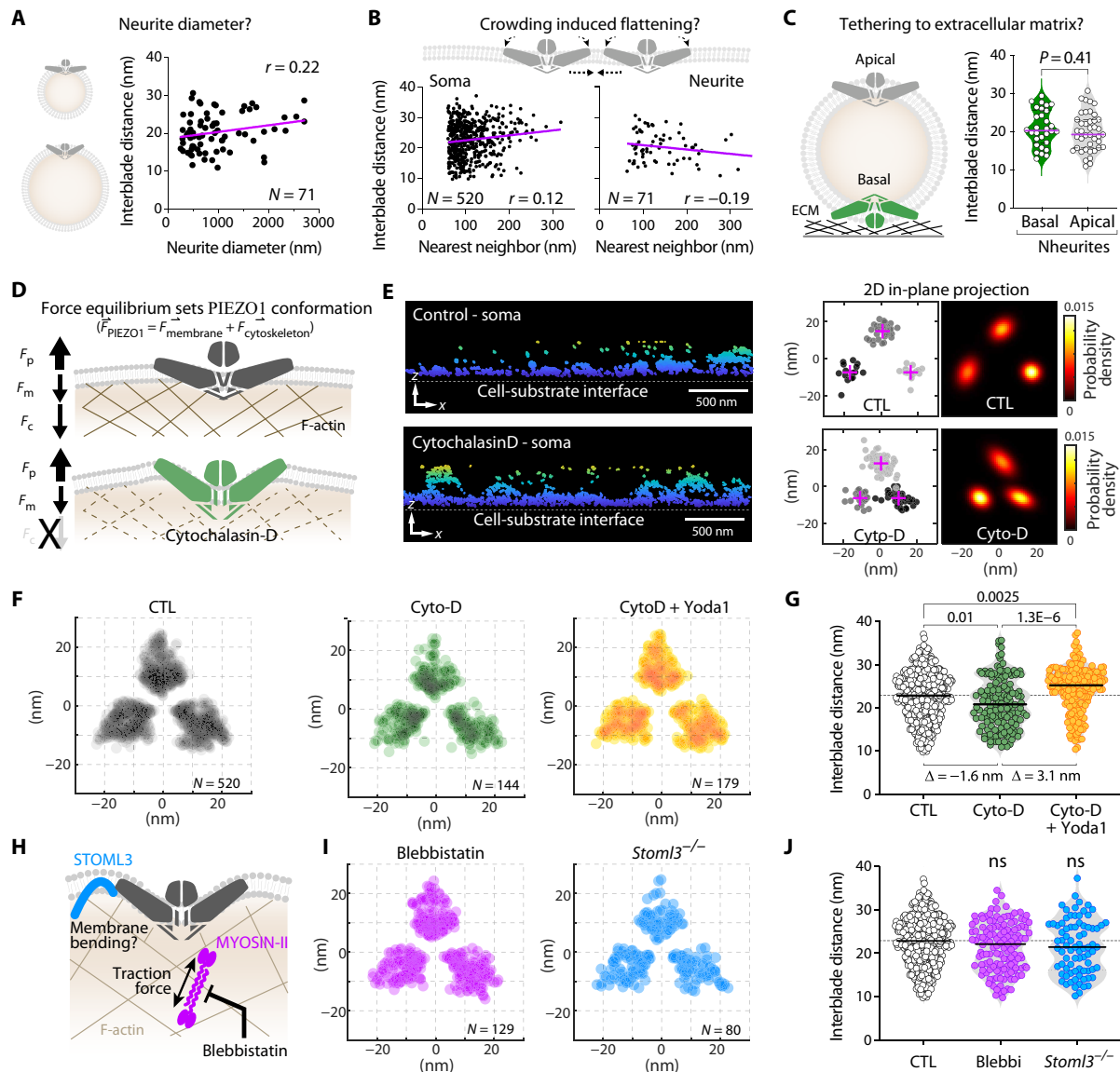


Fig. 2. Disruption of the cytoskeleton alters PIEZO1 conformation. (A) Relationship between neurite diameter and interblade distance in PIEZO1 trimers. (B) Correlation between interblade distance average distance to the three nearest neighbors of PIEZO1 trimers in somata and neurites. In (A) and (B), Pearson correlation coefficients “*r*” are indicated, and linear regressions are shown in pink. (C) Cartoon illustrating the possible effect of the ECM in neurites (left) and comparison of interblade distances between trimers located at the basal and apical side of neurites using Mann-Whitney test (basal: 20.9 ± 4.7 , $N = 30$; apical: 19.9 ± 4.9 , $N = 41$; $P = 0.41$). (D) Cartoon showing possible interplay of forces exerted by and acting on PIEZO1. (E) Side views of MINFLUX raw localization data from indicated conditions as well as in-plane projections of the raw localization data (middle) and 2D heatmaps of the localization probability densities (right) of representative trimers from control and cyto-D-treated cells. (F) Overlays of all trimers from control (black), cyto-D (green), and cyto-D + Yoda1 (orange)-treated cells. (G) Comparison of interblade distances of trimers shown in (F) using Kruskal-Wallis test (CTL: 22.7 ± 5.6 nm, $N = 520$; CytoD: 21.2 ± 5.9 nm $N = 144$; CytoD + Yoda1: 24.27 ± 5.39 nm, $N = 179$; P values are provide in graph). (H) Cartoon depicting the possible effects of traction forces and Stoml3 on PIEZO1 conformation. (I) overlays of all trimers from blebbistatin-treated (purple) and *Stoml3*^{-/-} (blue) cells. (J) Comparison of interblade distances from control (22.7 ± 5.6 nm, $N = 520$), blebbistatin-treated (purple; 21.5 ± 5.7 nm, $N = 129$) and *Stoml3*^{-/-} (blue; 21.56 ± 6.2 nm, $N = 80$) cells using Kruskal-Wallis test.

trimer identification rules only consider trimers with nearest neighbors that are more than 60 nm away, and thus the effect of dense clustering on channel conformation could not be tested. A possible confounding factor of our data is the imaging depth of MINFLUX, which is limited to a few hundred nanometers such that the apical surface of the cell soma cannot be imaged. Accordingly, all trimers that were detected in somata resided at the cell-substrate interface, where the channels could possibly be tethered to the extracellular matrix (ECM), whereas in neurites, trimers were detected in the basement membrane as well as in the apical membrane. In the experimental conditions used here [poly-L-lysine (PLL)-coated coverslips], there was no difference between the interblade distances of trimers in the basement membrane of neurites compared to those residing in the apical membrane, indicating that possible tethering of PIEZO1 to the ECM or lack thereof in the apical membrane does not alter PIEZO1 conformation (Fig. 2C). We can, however, not rule out that other matrix proteins such as laminin, fibronectin, and collagen, which preferentially engage different integrin receptors may differentially alter PIEZO1 conformation, considering that, for example, laminin-332 was shown to coordinate mechanotransduction in primary sensory neurons (46).

Since neither membrane curvature nor crowding or extracellular tethering appeared to account for the differences in PIEZO1 conformation between neurites and somata, we next considered the role of the cytoskeleton. The plasma membrane is tightly attached to the cytoskeleton, suggesting that the extent to which PIEZO1 deforms the membrane into a dome shape—and thus its own conformation at rest—may be controlled by the equilibrium of forces that PIEZO1 exerts on the membrane and the opposing forces that the membrane together with the cytoskeleton exert on PIEZO1 (Fig. 2D). Since neurites have a different overall cytoskeletal architecture with fewer membrane-cytoskeleton attachments (47–50) and PIEZO1 appears more contracted there (Fig. 1, D and E), we hypothesized that differences in local membrane deformability between neurites and somata contribute to the observed differences in PIEZO1 conformation in the two compartments. To test this hypothesis, we treated cells with the actin polymerization inhibitor cytochalasin-D (2 μ M cyto-D), which removes “mechanoprotection” and hence possibly renders the membrane more deformable (19, 51). As previously reported (19), this increased PIEZO1 current amplitudes and shifted the pressure-response curve toward less negative pressures (CTL: -40.5 ± 11.3 mmHg versus cyto-D: -29.1 ± 10.5 mmHg; fig. S6, A to C). Notably, cyto-D treatment significantly reduced the mean interblade distance of somatic PIEZO1 trimers (CTL: 22.7 ± 5.6 nm versus cyto-D: 21.2 ± 5.9 nm, $P = 0.01$, Kruskal-Wallis test; Fig. 2, E to G) and altered their conformational distribution, with fewer channels in the flattened and more channels in the curved state, mirroring the distribution in neurites (compare Fig. 2F with Fig. 1D). Considering the similarity of PIEZO1 interblade distance distributions in neurites and cyto-D-treated somata together with the fact that PIEZO1 in neurites was more sensitive to Yoda1 (Fig. 1F) and that cyto-D treatment increased the sensitivity of somatic PIEZO1 (fig. S6), we next asked whether Yoda1-induced channel flattening was also more pronounced after removal of mechanoprotection. In cyto-D-treated cells, Yoda1 caused a pronounced shift in the mean interblade distance by more than 3 nm (CytoD: 21.2 ± 5.9 nm versus CytoD + Yoda1: 24.27 ± 5.39 nm, $P = 1.3 \times 10^{-6}$, Kruskal-Wallis test), thereby increasing the proportion of flattened channels while reducing the number of curved channels (Fig. 2, F and G).

In summary, these data showed that the cytoskeleton plays a crucial role in controlling PIEZO1 conformation at rest but it remains unclear whether the effect of cyto-D treatment results from reduced cytoskeletal rigidity, which may facilitate membrane deformation and hence allow PIEZO1 to contract more, or form a loss of traction forces (i.e., nonmuscle myosin-II-dependent contractions of the actin cortex), which were previously shown to activate PIEZO1 (30)—supposedly by generating local membrane tension—and may thus be responsible for the observed partial flattening of PIEZO1 at rest. Incubation of cells with 30 μ M of the myosin-2 inhibitor blebbistatin did, however, not change the mean interblade distance of PIEZO1 (Fig. 2, H to J), suggesting that membrane deformability but not basal traction force is a major determinant of PIEZO1 conformation at rest. With regard to membrane deformability and PIEZO1 function, stomatin-like protein 3 (STOML3) is an intriguing protein as it was shown to sensitize PIEZO1- and PIEZO2-mediated currents in N2a cells and primary sensory neurons (52–54), possibly by membrane stiffening, and members of the stomatin protein family were proposed to cause membrane bending. To test whether STOML3, which is expressed in N2a cells, alters PIEZO1 conformation at rest, we generated an N2a-STOML3 knock-out cell line using CRISPR-Cas9 technology (fig. S6, D to F) and measured interblade distances of recombinantly expressed PIEZO1 in these cells. Although the mean interblade distance was slightly reduced in N2a-STOML3 knockout (KO) cells (21.6 ± 6.2 nm, $N = 80$) as compared to control measurements in N2a-P1KO cells (22.7 ± 5.7 nm, $N = 520$), this difference was statistically not significant ($P = 0.288$, Kruskal-Wallis test; Fig. 2, H to J). Together, our data show that the cytoskeleton governs PIEZO1 conformation at rest, possibly by fine-tuning the deformability of the plasma membrane at the nanoscale.

PIEZO1 adopts discrete conformations in its native environment

A recurring observation in our experiments was that the interblade distances were scattered across a wide range and were not normally distributed (Figs. 1E and 2, G and J), which was puzzling at first glance, considering the high spatial resolution and localization precision of 3D-MINFLUX (fig. S3C). However, in addition to the curved conformation, which was described by several laboratories (15–17), the Xiao laboratory has resolved an intermediate and possibly partially open state, in which the blade domains are tilted downward (14) as well as a fully flattened conformation, which may represent an open or inactivated state (7). Moreover, using in silico computational modeling, Smith and colleagues (55) recently described a phenomenon called “handshaking,” which refers to interactions between the distal end of one blade with the proximal THU8 of the neighboring blade, and propose that single, double, and triple handshaking can stepwise decrease the mean interblade distance of the curved PIEZO1 conformation. Thus, at least six discrete conformational states of PIEZO1 may exist (Fig. 3A), which could explain the broad and nonuniform distribution of interblade distances.

In agreement with this hypothesis, a Gaussian mixture model with six components faithfully fitted the interblade distance distribution of our large control dataset (soma-CTL, $N = 520$, $R^2 = 0.937$; Fig. 3B), with four peaks at 21.7, 18.2, 15, and 11.5 nm, which may represent channels in the curved conformation with either zero, one, two, and three handshakes, respectively, and two additional peaks at 26.2 and 30.8 nm, which may correlate with the intermediate and fully flattened PIEZO1 conformation. We also attempted to fit the interblade

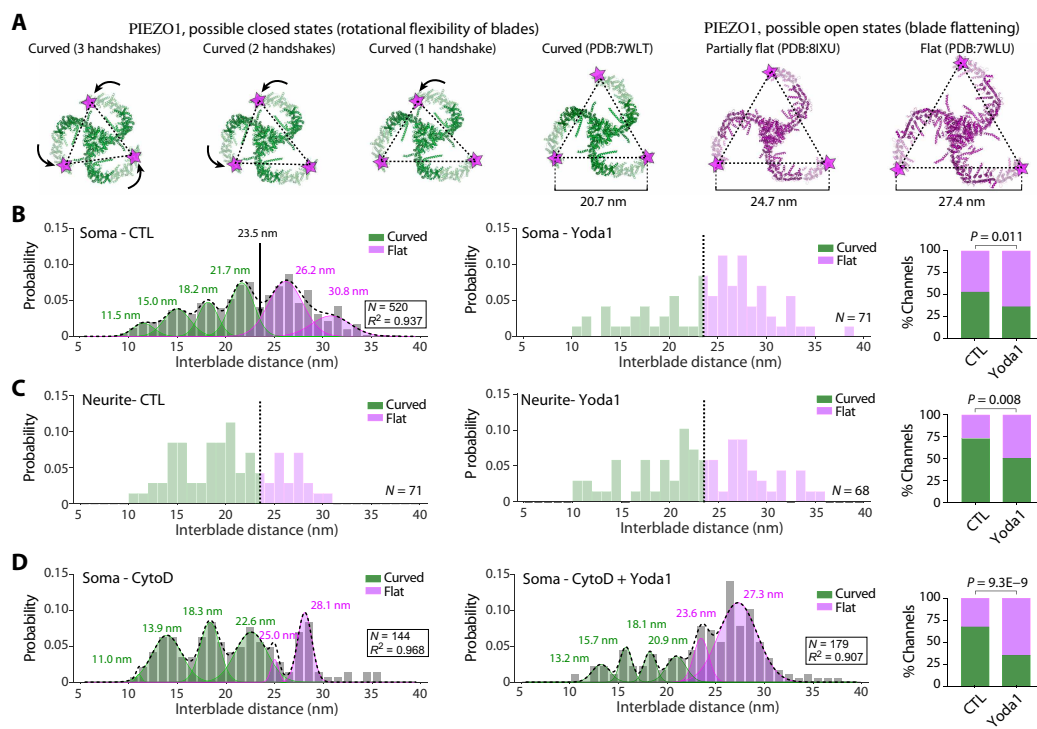


Fig. 3. PIEZO1 adopts discrete conformations in its native environment. (A) Top views of the indicated cryo-EM structures of possible closed (green) and open states of PIEZO1. To enable depiction of interblade distances, the peripheral ends of the blade domains, which were not resolved by cryo-EM, were modeled by aligning the full-length AlphaFold structure (AF-E2JF22) with cryo-EM structures. Domains originating from the AlphaFold structure are shown as semitransparent cartoons. To illustrate handshaking between adjacent blades, the peripheral blades were manually rotated counterclockwise. (B) Interblade distribution histograms (bin size, 1 nm) of all trimers detected in somata in the absence (soma - CTL) and presence (soma - Yoda1) of Yoda1. The distribution of control trimer interblade distances was fitted with a Gaussian mixture model with six components. Peaks that possibly represent curved conformation (included curved with handshaking) are shown in green and those representing flat states (partially and fully flattened) in purple. 23.5 nm was chosen as a cutoff for classifying channels as curved or flat because this was the interblade distance at which the subdistributions of the supposedly curved conformation with the largest mean interblade distance (21.7 nm, zero handshakes) and the partially flattened conformation (mean = 26.2) intersected. The bar graph shows a comparison of the proportions of curved and flattened channels in the absence (CTL) and presence of Yoda1 using Fisher's exact test. (C) and (D) show interblade distribution histograms of PIEZO1 trimers detected in neurites (C) and cyto-D-treated cells (D) in the indicated conditions (left and middle) and comparisons of the proportions of curved and flattened channels in the absence (CTL) and presence of Yoda1 using Fisher's exact test. Note that in some experimental conditions, specific conformations were underrepresented, which precluded meaningful fitting and thus these distributions were only categorized into curved (green) and flat (light purple).

distributions detected in other experimental conditions, but because of differences in sample size, we only obtained additional meaningful fits for trimers detected in the presence of cyto-D and cyto-D plus Yoda1. In all other distributions, we thus solely classified channels as curved and flat when their interblade distances were smaller or greater than 23.5 nm, respectively. We chose the cutoff of 23.5 nm because this was the interblade distance at which the subdistributions of the supposedly curved conformation with the largest mean interblade distance (21.7 nm, zero handshakes) and the partially flattened conformation (mean = 26.2) intersected in the control dataset (Fig. 3B) and because it fell between the interblade distances estimated from the curved and partially flattened (intermediate open) cryo-EM structures (Fig. 3A). This classification into curved and flat channels revealed that Yoda1 significantly increases the proportion of flat channels as compared to the respective control datasets (bar graphs in Fig. 3, B to D) across all tested conditions. Moreover, it showed that significantly more channels adopt a curved conformation in neurites (52 curved versus 19 flat; $P = 0.0014$, compared with CTL using Fisher's exact test) and after disruption of the cytoskeleton with cyto-D (97 curved versus 47 flat; $P = 0.0024$, compared with

CTL using Fisher's exact test) as compared to controls (276 curved versus 244 flat). Last, the Gaussian mixture model fits of the distributions of trimers detected in the presence of cyto-D and cyto-D plus Yoda1 exhibited multiple clearly discernible peaks with means that were similar to those of the control dataset fit, suggesting that PIEZO1 adopts discrete conformations in its native environment rather than existing in a continuum of gradually curved and flattened states.

PIEZO1 forms clusters that mediate local calcium influx

The data described so far exclusively focused on PIEZO1 channels that resided in isolation. As evident from anti-ALFA MINFLUX scans (Figs. 1C, 2E, and 4A) as well as from confocal scans of mGL fluorescence (Fig. 4A), and as previously reported (20, 26, 27, 29–35, 56); however, PIEZO1 channels are not uniformly distributed across the cell surface but also form prominent clusters that appear to be densely packed with multiple channels. To corroborate previous reports regarding cluster formation, we first examined the distribution of endogenously expressed PIEZO1 in mouse embryonic fibroblasts (MEFs) and U87 human glioblastoma cells using immunocytochemistry and

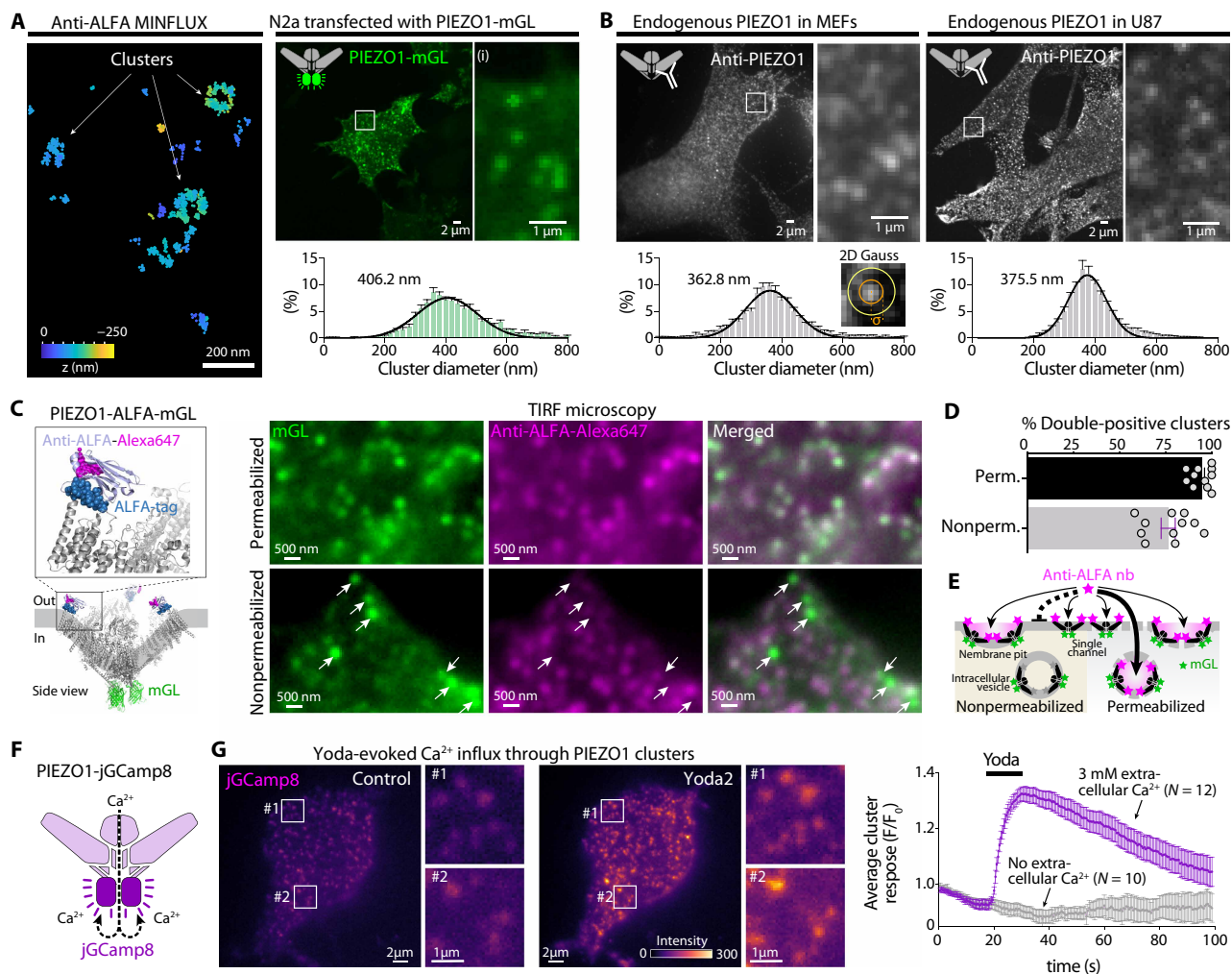


Fig. 4. Endogenous and transiently expressed PIEZO1 forms functional cluster at the plasma membrane. (A) Example of 3D-MINFLUX raw localization data from extracellular ALFA tag–labeled PIEZO1 (left), highlighting the presence of PIEZO1 clusters. Representative TIRF image of N2a-P1KO cell transfected with PIEZO1-mGL with close-up of marked region (top right) and histogram showing the distribution of cluster diameters (bottom) with associated Gaussian fit and average. (B) Representative TIRF images (top) of endogenous PIEZO1 clusters labeled with an anti-PIEZO1 antibody in MEF (left) and U87 (right) cells, with corresponding PIEZO1 cluster diameter distribution (bottom). (C) Cartoon depicting the position of the extracellular ALFA tag with its nanobody conjugated to Alexa Fluor 647 and intracellular mGL in PIEZO1-ALFA-mGL (left). Representative TIRF images of PIEZO1-ALFA-mGL transfected N2a-P1KO cells permeabilized (top) or not permeabilized (bottom) and labeled with Alexa Fluor 647–coupled nanobody against ALFA tag (right). Scale bar, 500 nm. (D) Comparison of the proportion of PIEZO1 clusters double positive for mGL and ALFA-Alexa Fluor 647 per cell analyzed ($N = 11$ cells for both conditions, presented as means \pm SEM). Two-tailed unpaired t test, $P = 0.0003$. (E) Schematic representation of the accessibility of ALFA-tagged PIEZO1 channels and clusters depending on the permeabilization status of the cell. (F) Cartoon depicting the PIEZO1-jGCaMP8m fusion protein. (G) Representative TIRF images (left) of N2a-P1KO cells expressing PIEZO1-jGCaMP8m with close-up views of PIEZO1 clusters before and during Yoda2 application. Time-course of the cell-average cluster normalized jGCaMP8m fluorescence (F/F_0) upon application of Yoda2 with (384 clusters, 12 cells) and without extracellular calcium (174 clusters, 10 cells).

total internal reflection fluorescence (TIRF) microscopy. In both cell lines, immunofluorescence signals were scattered across the plasma membrane and appeared as discrete puncta with mean diameters of 362.8 ± 81.3 nm (MEFs) and 375.5 ± 62.2 nm (U87; Fig. 4B), indicating that PIEZO1 also forms clusters at endogenous expression levels that were indistinguishable with regard to size and density from the clusters observed in N2a cells recombinantly expressing PIEZO1-ALFA-mGL (406.2 ± 97.9 nm; Fig. 4A and fig. S7A). Consistent with this observation, mechanically evoked currents produced by recombinantly expressed PIEZO1 in N2a-P1KO cells were only slightly bigger than endogenous PIEZO1 currents in MEFs (fig. S7B), demonstrating that recombinant expression levels of

PIEZO1 in N2a cells were within the physiological range. Immunolabeling of unpermeabilized N2a cells expressing PIEZO1-ALFA-mGL with a nanobody directed against the extracellularly located ALFA tag further demonstrated that $76.5 \pm 12.7\%$ of the mGL-positive clusters were embedded in the plasma membrane, whereas only a small proportion appeared to be intracellular vesicles (Fig. 4, C to E). To examine the functional relevance of PIEZO1 clusters, we generated a PIEZO1-jGCaMP8m fusion protein in which the genetically encoded calcium sensor jGCaMP8m was located adjacent to the intracellular exit of the ion conduction pathway such that local PIEZO1-mediated calcium influx can be detected (Fig. 4F and fig. S8). Consistent with previous reports using similar approaches

(34, 38), stimulation of PIEZO1-jGCamp8m expressing N2a-P1KO cells with the PIEZO1 activator Yoda2 (57) produced discrete Ca^{2+} signals in clusters, which were abolished in the absence of extracellular calcium (Fig. 4G and movie S3).

Hence, our data together with previous reports show that endogenously (26, 29, 31–35) and recombinantly expressed PIEZO1 (20, 27, 30, 33, 56) forms clusters that contain functional channels, which possibly contribute to cellular mechanosensitivity (34, 38) (Fig. 4G).

PIEZO1 clusters form pit-shaped invaginations in the plasma membrane

The unequivocal identification of trimers in densely packed clusters is challenging because adjacent and partially labeled trimers may produce signal triplets that are indistinguishable from “truly” triple-labeled PIEZO1 trimers (Fig. 5A). To circumvent this problem and to obtain more reliable information about the nanoarchitecture of PIEZO1 clusters as well as the absolute number of channels and their relative position within clusters, we next performed 3D-MINFLUX/DNA-PAINT scans using a single-domain nanobody that recognizes the intracellular mGL tags, which are much closer together such that individual channels are clearly discernible even when partially labeled (Fig. 5A and fig. S9, A to C for negative controls). The anti-mGL 3D-MINFLUX localization data perfectly matched the mGL fluorescence pattern in confocal images and resolved individual fluorophores with a localization precision of less than 3 nm in all three dimensions (Fig. 5, B to D), which revealed that clusters contain multiple channels and that many channels appear to reside in isolation in the interjacent space (Fig. 5C). To estimate the proportion of isolated channels, we quantified the number of channels that did not have any neighbors within their membrane footprint using previously proposed hypothetical footprint radii between 50 and 100 nm (6, 11, 12, 58). This analysis suggested that, depending on the assumed footprint radius, 16.9 to 44.7% of the channels are isolated and 32.8 to 74.5% only have a single neighbor within their footprint (Fig. 5E), demonstrating that despite the prominence of clusters, a considerable fraction of PIEZO1 channels reside in isolation.

Most notably, our 3D-MINFLUX scans revealed previously unrecognized details about the nanoarchitecture of PIEZO1 clusters, which appeared as ring-like structures in the 2D-projected MINFLUX data (Fig. 5C). Closer inspection of the MINFLUX localization data in 3D showed that all clusters exhibited significant expansion along the z axis, with most clusters having a clearly recognizable pit-like shape, while others appeared to be spherical objects (Fig. 5, F and G, and movies S4 and S5). To quantify the proportions of pit-shaped and spherical clusters, we segmented the raw MINFLUX localization data of each cluster into signals originating from the upper fifth (top) and the lower four fifth (bottom) (Fig. 5F) and classified clusters in which no channels were present near the center of the top segment as pit-shaped clusters, whereas those clusters that did contain channels in this region were considered as spherical clusters (Fig. 5G). Consistent with the results from the anti-ALFA labeling of unpermeabilized cells (Fig. 4D), this classification scheme suggested that approximately two-thirds of the PIEZO1 clusters were pit-shaped and had direct access to the extracellular side (62.9%, 158 from 251), while the remaining third appeared to be spherical and possibly located intracellularly (93 from 251 clusters; Fig. 5, H and I). The pit-shaped clusters had a depth of 144 ± 60.1 nm, a radius of 72.8 ± 27.3 nm, and contained an average of 23.1 ± 11.3 channels (Fig. 5, J and K).

Previous studies have shown that PIEZO1 enriches in concave environments such as the dimple region of red blood cells (36), T-tubules in cardiomyocytes (32), and in nanoscale invaginations formed by cells grown on nanobars (59), which raises the question whether cluster formation results from the accumulation of channels in preexisting invaginations or whether PIEZO1 actively contributes to membrane bending and pit formation. The PIEZO1-pits observed here were reminiscent of other well-described pit-shaped invaginations, such as clathrin-coated pits, caveolae, and intermediate stages of vesicle formation (e.g., COP1-coated cargo vesicles) (60–62). To examine whether PIEZO1 clusters colocalize with these invaginations, we cotransfected N2a-P1KO cells and MEFs with PIEZO1-mScarlet (fig. S10, A to I) and clathrin-mGL and immunolabeled the cells with antibodies directed against caveolin-1 and COP1, respectively (Fig. 6A). The great majority of PIEZO1 clusters did not colocalize with these invagination markers, neither in N2a-P1KO cells nor in MEFs (Fig. 6A). The only exception was a 17.6% overlap of PIEZO1 clusters with clathrin-coated pits in N2a cells. However, consistent with a prior report (27), blocking clathrin-dependent endocytosis with 75 μM Dynasore did not change the density of PIEZO1 clusters in the plasma membrane observed in living cells via TIRF microscopy, suggesting that clathrin is not required for PIEZO1-pit formation (Fig. 6B). Hence, neither clathrin nor caveolin-1 or COP1 appear to be required for PIEZO1-pit formation and, vice versa, and PIEZO1 is dispensable for the formation of clathrin-coated pits, caveolae, and COP-coated vesicles as these invaginations are also formed at similar densities in N2a-P1KO cells lacking PIEZO1 (fig. S10, J to K). Moreover, PIEZO1 cluster formation was neither affected by inhibition of traction forces with blebbistatin and disruption of the cytoskeleton with cyto-D nor by the lack of STOML3, as evidenced by prominent labeling of clusters with an anti-ALFA nanobody in unpermeabilized N2a-P1KO and N2a-Stoml3KO cells recombinantly expressing PIEZO1-ALFA-mGL (Fig. 6C).

Hence, in summary, our data demonstrate, that PIEZO1-pits are distinct from classical membrane invaginations such as clathrin-coated pits, caveolae, and COP1-coated invaginations and are formed independent of perturbations in cytoskeletal integrity, traction forces and Stoml3. We cannot rule out that other, yet unknown, accessory proteins or lipids are required for PIEZO1-pit formation, but considering that individual PIEZO1 channels were shown to locally deform the membrane into a dome shape (12) and given the remarkable structural similarity between PIEZO1, clathrin, and COP1 (Fig. 6D), it is tempting to speculate that PIEZO1 channels actively contribute to pit formation due to their curved triskelion structure, which appears to be a common feature of coat proteins that are required for pit formation in other biological processes (63, 64).

Hypoosmotic stimulation alters PIEZO1 cluster nanoarchitecture

PIEZO1 is activated by changes in membrane curvature and tension evoked by mechanical stimuli such as membrane stretch, cell compression, and hypotonic stress-induced cell swelling (2, 4, 5). We thus examined how the pit-shaped microenvironment of PIEZO1 clusters changes in response to mechanical stimulation by comparing the PIEZO1 cluster nanoarchitecture of cells fixed during hypoosmotic stimulation with that of control cells. Exposure of PIEZO1-mGL-expressing N2a-P1KO cells to hypoosmotic stress before and during fixation, significantly reduced the depth of pit-shaped clusters (CTL: 144 ± 60.1 nm versus OSMO: 110.7 ± 54.8 nm; Fig. 7, A to C; movies S6

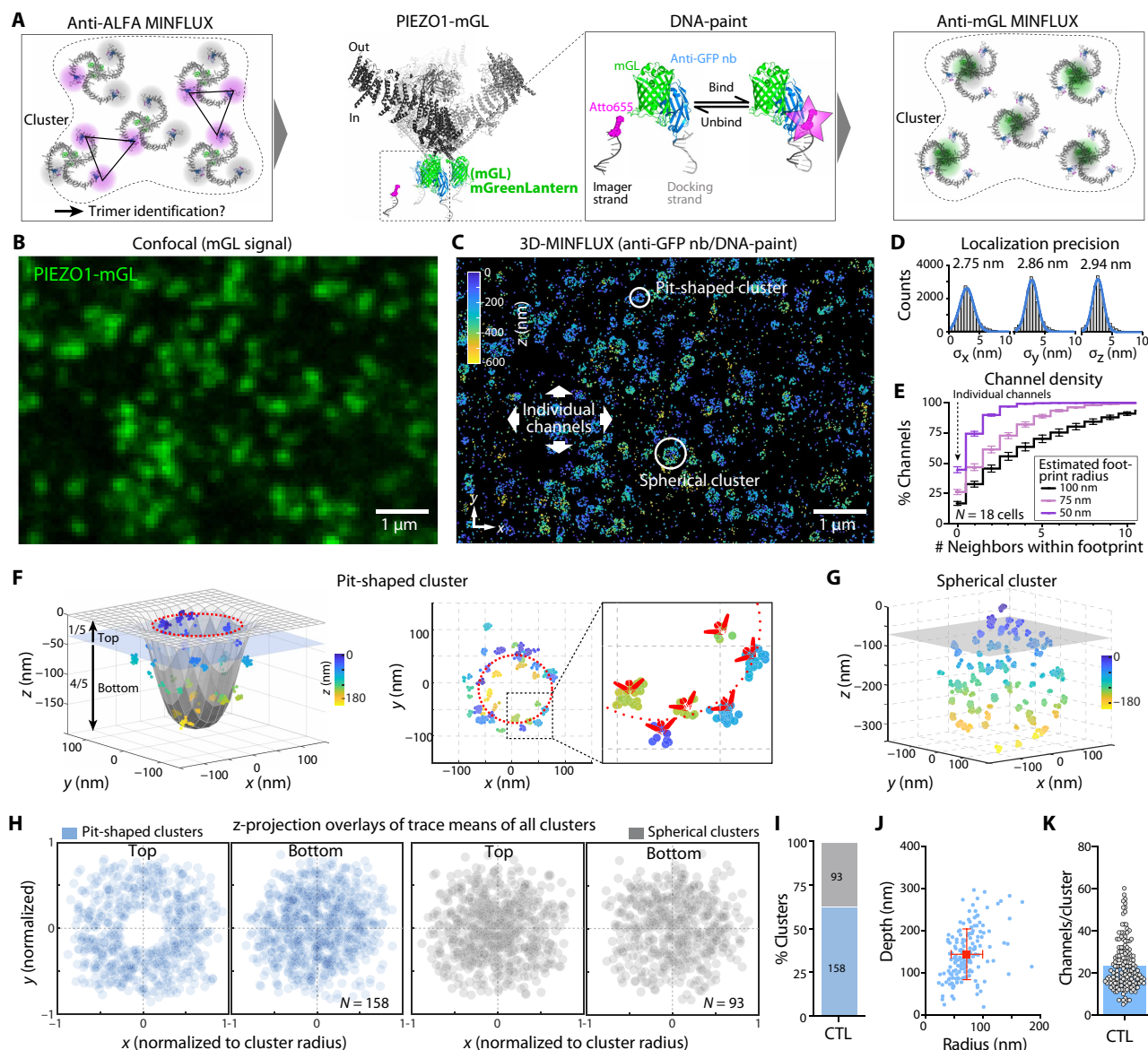


Fig. 5. 3D-MINFLUX reveals pit-shaped nanoarchitecture of PIEZO1 clusters. (A) Cartoon highlighting complication of trimer identification in ALFA-labeled PIEZO1 clusters (left), PIEZO1 structure depicting the mGL-tag position with DNA-PAINT approach (middle) to improve PIEZO1 channel identification within clusters (right). (B) Confocal scan of N2a-P1KO cell expressing PIEZO1-mGL. (C) Corresponding 3D-MINFLUX localization data colored by z position. (D) Distribution of the MINFLUX trace SDs along the indicated axis. (E) Cumulative distributions of the percentages of PIEZO1 channels (y axis) with the indicated number of neighbors (x axis) within their membrane footprint, calculated for different possible footprint radii (100 nm, black; 75 nm, light purple, 50 nm, dark purple). Note that depending on the assumed footprint radius, between 16.9 and 44.7% of PIEZO1 trimers have zero neighbors and are considered as “individual” channels (marked by arrow). (F) 3D (left) and top view (left) of MINFLUX localization data of the pit-shaped cluster marked in (C). The inset shows the putative localization of individual PIEZO1 channels within the cluster. (G) 3D view of MINFLUX localization data of the spherical cluster marked in (C). For 360° rotation movies of clusters in (F) and (G); see movies S4 and S5. (H) Overlay of 2D projections of the traces means of the top fifth (top) and bottom four-fifth (bottom) of all pit-shaped clusters (blue circles, $N = 158$ cluster from 19 cells) and spherical clusters (gray circles, $N = 93$ clusters from 19 cells). Note that in pit-shaped clusters, no channels are present at the top center. (I) Bar graph showing proportions of pit-shaped and spherical clusters. (J) Relationship between cluster depth and width of individual pit-shaped cluster (blue dots) with means \pm SEM shown in red. (K) Bar graph (mean) with scatter plot (circles) showing the number of channels per cluster.

and S7; and fig. S11), yet the proportions of pit-shaped and spherical clusters were not changed (Fig. 7D). There was also a slight decrease in the average number of channels per cluster but no change in the pit opening radius (Fig. 7, E and F). Considering that PIEZO1 is supposedly activated by changes in membrane curvature and considering further that pit-shaped invaginations exhibit a strong gradient

of curvatures ranging from positive values (concave) at the bottom to negative values (convex) at the pit opening (Fig. 7B), small changes in cluster structure or in the relative localization of channels within the pits could have large effects on the curvature that individual channels are exposed to and hence on their activity. We thus fitted the surface of the clusters and calculated the Gaussian curvature of

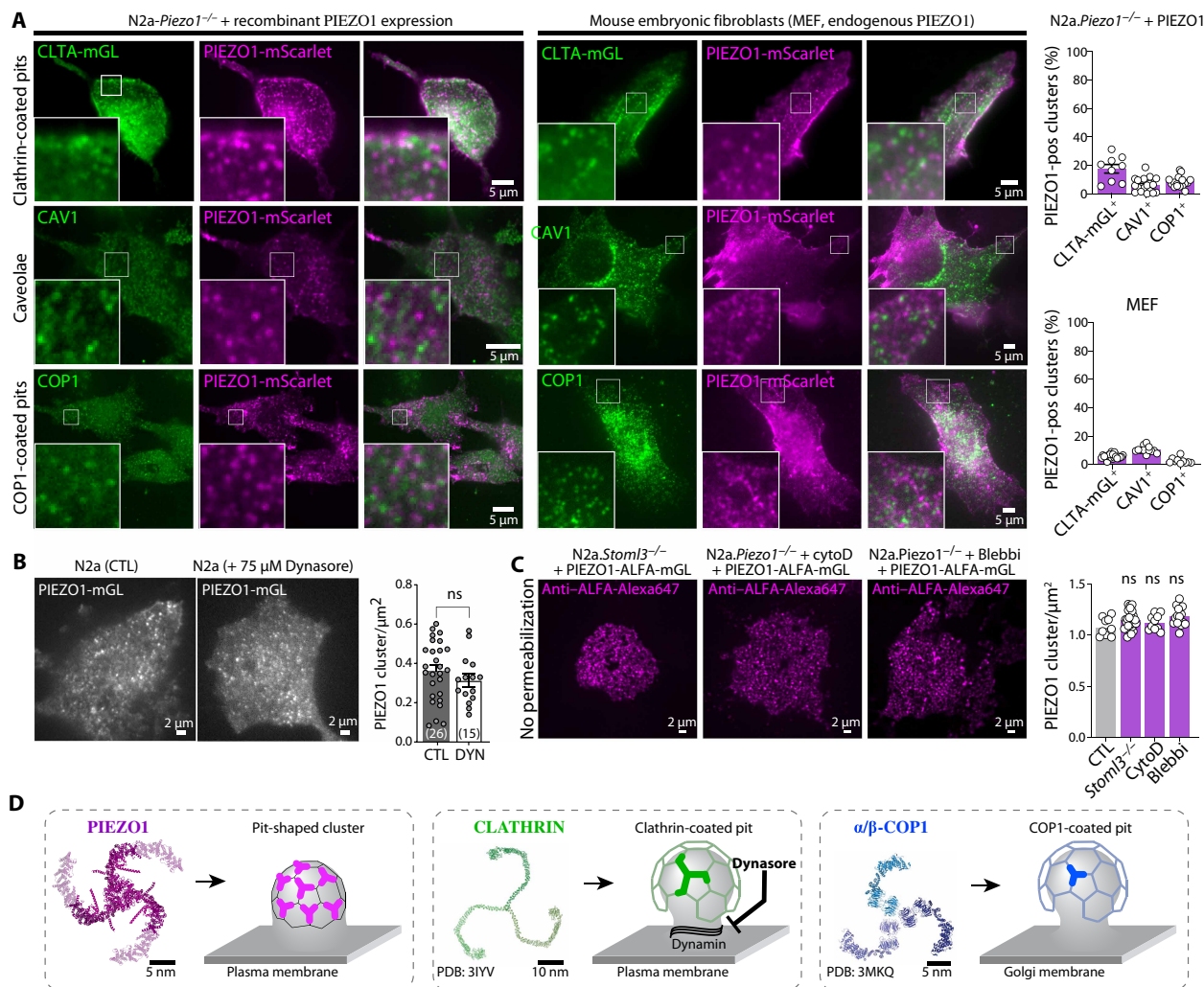


Fig. 6. PIEZO1 pit-shaped clusters are distinct cellular invagination structures. (A) Representative TIRF images of PIEZO1-mScarlet expressed in N2a-P1KO (left) and MEF (right) together with clathrin light chain-mGL to visualize clathrin-coated pits and colabeled with Cav1 (caveolae) or α COP1 (COP1-coated pits). Bar graphs show quantifications of the proportion of PIEZO1 clusters expressing the cellular invagination markers in N2a-P1KO (top right) and MEF (bottom right) cells. Data are presented as cell average. (B) Representative TIRF images (left) of N2a-P1KO live cells expressing PIEZO1-ALFA-mGL and extracellularly labeled with anti-ALFA-Alexa Fluor 647 nanobodies with or without the clathrin-dependent endocytosis inhibitor Dynasore. Quantification (right, presented as cell average) of the number of PIEZO1 clusters. Two-tailed unpaired *t* test, *ns* $P = 0.3141$. (C) TIRF images of PIEZO1-ALFA-mGL labeled with anti-ALFA-Alexa Fluor 647 nanobodies and without permeabilization expressed in N2a-*Stoml3*-KO cells (left), N2a-P1KO cells treated with cyto-D (middle), and N2a-P1KO cells treated with blebbistatin (right). Bar graph shows the number of extracellularly labeled PIEZO1 clusters in the indicated conditions, demonstrating that neither treatment affected cluster formation. (D) Cartoon depicting the structural similarity of PIEZO1 pit-shaped cluster (left, PDB 7WLT with AFE2JF22F1, shaded) with other pit/invagination-related proteins: clathrin (middle) and the $\alpha\beta$ subunits of the COP1 complex (right).

the surface at the coordinates where individual channels were detected. This analysis revealed that the mean curvature that individual channels are exposed to is significantly reduced during hypoosmotic stimulation and that more channels are exposed to convex curvatures in which they are more likely to be open (Fig. 7G). Together, our data suggest that pit-shaped invaginations change their shape in response to hypoosmotic stimulation resulting in changes in local curvature and possibly activation of individual channels.

DISCUSSION

A recent MINFLUX study suggested that PIEZO1 is generally more expanded in its native environment than predicted by cryo-EM

structures of PIEZO1 reconstituted in liposomes (23). Our work extends and refines these findings by showing that PIEZO1 in intact cells assumes discrete conformations closely matching known cryo-EM structures and that the preference for specific conformations varies between subcellular compartments (Fig. 1, C to E). We also identify the cytoskeleton as a crucial cell intrinsic factor that differentially controls PIEZO1 conformation at rest across subcellular compartments (Fig. 2). Last, we observed compartment-specific differences in PIEZO1’s susceptibility to Yoda1-induced flattening, which correlate with differences in mechanical and chemical sensitivity (Fig. 1F).

Analysis of the interblade distance distribution of PIEZO1 channels in somata using a Gaussian mixture model revealed that interblade

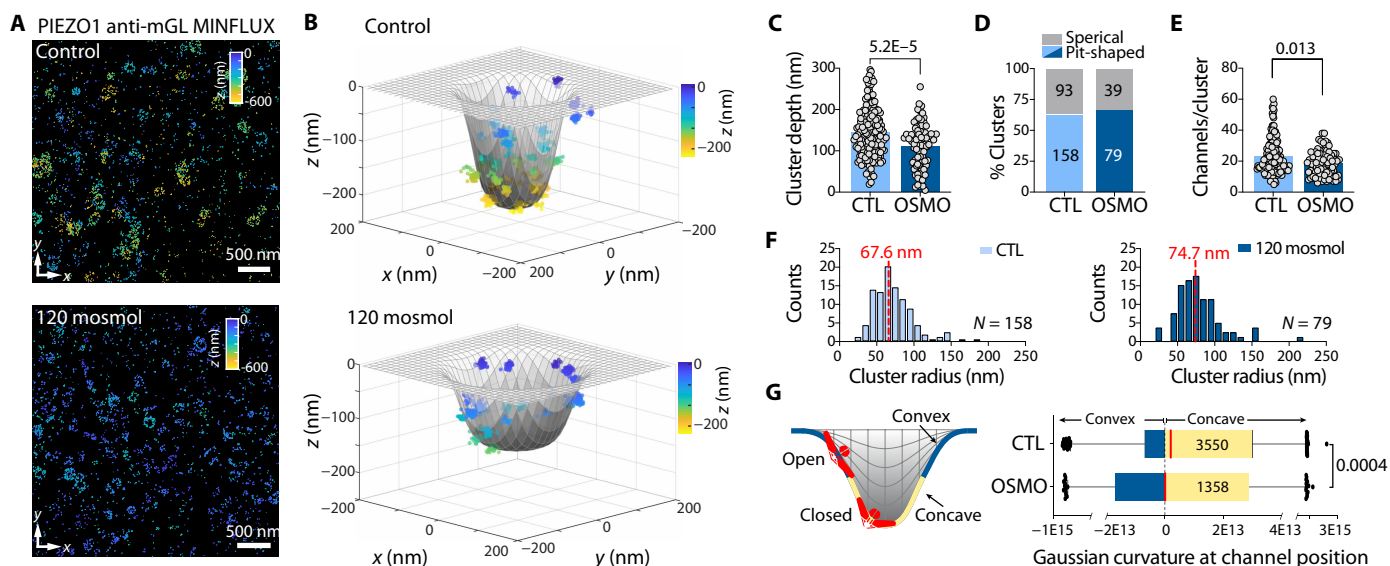


Fig. 7. Hypoosmotic stimulation causes partial flattening of pit-shaped clusters. (A) Raw MINFLUX localization of clusters imaged in control cells (top) and challenged with hypoosmotic solution (bottom). (B) 3D views of the raw MINFLUX localization of representative clusters from control (top) and osmotically stimulated (bottom) cells together with surface fits. (C) Comparison of the cluster depths (CTL: $N = 158$ versus OSMO: $N = 79$, $P = 0.000052$, two-tailed Student's t test). (D) Proportions of pit-shaped (blue) and spherical clusters (gray) in control (CTL) and hypoosmotically stimulated (OSMO) cells. Absolute numbers of clusters are within the bar. (E) Comparison of the means \pm SEM number of PIEZO1 channel found in individual pit-shaped clusters. (CTL: $N = 158$ versus OSMO: $N = 79$, $P = 0.0134$, two-tailed Mann-Whitney test). (F) Histograms of the radii of all pit-shaped clusters measured at the pit opening. Medians are indicated in red. (G) Schematic surface fit in which convex regions are depicted in blue, and concave regions are shown in yellow (left). The possible impact of curvature on PIEZO1 (red) conformation is depicted. Gaussian curvatures of the fitted surfaces [see (B)] calculated at the coordinates where channels are and shown as horizontal box plots, ranging from the lower quartile to the upper quartile. Medians are shown as red lines. Mean curvatures were compared using Mann-Whitney test ($P = 0.0004$, $N = 3550$ for CTL and $N = 1358$ for OSMO).

distances are not uniformly distributed, suggesting that PIEZO1 preferentially adopts discrete and possibly energetically favorable conformations rather than existing in a continuum of gradually curved and flattened states. (Fig. 3). This hypothesis is in agreement with previous cryo-EM studies that described three distinct PIEZO1 structures—i.e., a curved (15–17), a partially flattened (14), and a fully flattened (7) conformation—with interblade distances that closely match the interblade distances measured here for the three most expanded conformations (Fig. 3). Moreover, a preference for these three conformations, native cell membranes has been proposed by a recent preprint using single-particle cryogenic light microscopy of unroofed cells (65). With regard to the existence of four substates of the curved conformation, our data are consistent with the idea that the peripheral parts of the blades exhibit significant rotational flexibility, which has been described by Mulhall and colleagues (23) using iPALM and MINFLUX and is thought to be the reason why these domains could never be resolved by cryo-EM. Most recently, Smith *et al.* (55) described a phenomenon called handshaking that depends on membrane PIP2 and refers to the stabilization of interactions between neighboring blades. Notably, the blades can rotate independent of each other, thereby allowing the formation of multiple conformational substates with zero, one, two, or three handshakes. Of course, PIEZO1 transiently also exists in intermediate states as it switches between conformations, but the fact that clearly discernible peaks were evident in all interblade distance distributions analyzed here strongly suggests that certain states are more stable than others.

Regarding cell-intrinsic factors that stabilize certain conformational states, membrane curvature, extracellular tethering to the ECM, and channel crowding did not seem to play a major role (Fig. 2, A to C).

Likewise, inhibition of cell-generated traction forces and knockout of *Stoml3* did not alter PIEZO1 conformation at rest (Fig. 2, H to J). Disruption of the cytoskeleton with cyto-D, however, altered the distribution of PIEZO1 conformation such that it mirrored the distribution observed in neurites, indicating that differences in cytoskeletal architecture may contribute to the observed compartment-specific differences in PIEZO1 conformation (Fig. 2, D to G). This observation is consistent with the idea that PIEZO1 exerts a bending force onto the membrane (6, 8, 11, 12), which implicates that PIEZO1 can contract more in cell compartments and nanodomains in which the membrane is more deformable. Considering the membrane and the cytoskeleton as a composite material, the deformability of the membrane at the microscopic level does not only depend on the curvature and lipid composition of the membrane itself but also on cytoskeletal rigidity. Moreover, at the nanoscopic level, the membrane is compartmentalized by cytoskeletal attachments, which limit the lateral flow of lipids such that large membrane compartments created by widely spaced cytoskeletal attachments are more deformable than smaller compartments. Accordingly, modeling studies have proposed that these attachments may impose constraints on the size of PIEZO1s membrane footprint (6, 11)—i.e., the degree of PIEZO1 flattening. Neurites are well known to have a different overall cytoskeletal architecture with fewer membrane-cytoskeleton attachments (47–49) and were shown to be more deformable at the microscopic level (50, 66, 67). Likewise, cytoskeleton disruption with cyto-D reduces the bulk elastic modulus of the cell thereby possibly rendering the membrane more deformable (51). Moreover, elegant membrane tether pulling studies have shown that the membranes of somata are more resistant to lateral lipid flow than those of axons, possibly because of

differences in the density and spatial arrangement of membrane-cortex attachments (68, 69). Hence, together, our observations that PIEZO1 is more contracted in neurites and after disruption of the cytoskeleton with cyto-D support a model in which PIEZO1 conformation at rest is strongly influenced by local membrane deformability, which is controlled by cytoskeletal rigidity and possibly the density of membrane cytoskeleton attachments.

We also assessed how PIEZO1 conformation changes during Yoda1-induced activation. In somata, Yoda1 caused only minor, insignificant interblade expansion (Fig. 1E), as previously reported by Mulhall *et al.* (23). In neurites, which are more sensitive to Yoda1 (Fig. 1E), and after cyto-D treatment, which increases the mechanosensitivity of PIEZO1 (fig. S6), however, Yoda1 induced highly significant and much more pronounced changes in interblade distances (Figs. 1E and 2G). The simple interpretation of these results is that enhanced chemical and mechanical sensitivity correlates with a larger relative change in interblade distance. However, our detailed analysis of the interblade distributions suggested a more complex explanation. Thus, in the somata of control cells, almost 50% of the channels seem to adopt a flattened conformation (Fig. 3A), whereas only 25 and 32% of the channels were flat in neurites and after cyto-D treatment, respectively (Fig. 3, C and D). Because of the lack of precise side-chain density in the cryo-EM structure of the fully flattened conformation, it is unclear whether this conformation represents an open or an inactivated state (7, 14). Considering that 50% of the channels appear to be partially or fully flattened in the soma, yet spontaneous activity is rarely observed in patch-clamp recordings and calcium imaging, our data suggest that most flattened channels are probably in an inactivated state. Accordingly, it is tempting to speculate that curved channels (and curved substates with multiple handshakes), which are more abundant in neurites and after cyto-D treatment, are more susceptible to mechanical and chemical activation, which is consistent with our experimental observations. With regard to Yoda1-dependent activation, this hypothesis is further supported by recent studies suggesting that the Yoda1-binding site, which is supposedly located at the intracellular side of the THU8-THU9 interface (Fig. 1G) (45), may have a lower affinity or may not be available at all in the flattened state (70, 71).

In summary, our data highlight that PIEZO1 is not a rigid, binary switch but a conformationally plastic channel whose resting and activated conformations are dynamically tuned by the physical properties of its microenvironment, positioning the cytoskeleton as a key modulator of mechanosensitive signaling. Accordingly, our findings have significant implications for understanding compartmentalized mechanotransduction in neurons and other polarized cells and serve as a mechanistic framework for future studies that should aim to identify the molecular nature and spatial organization of membrane-cytoskeleton attachments that regulate PIEZO1 conformation.

In addition to investigating how the conformation of individual PIEZO1 channels is shaped by the native cellular environment and during channel activation, we also examined the subcellular distribution of PIEZO1 and the impact of clustering on membrane topology. Previous studies using immunolabeling, live-cell calcium imaging, and STORM superresolution microscopy have reported the presence of PIEZO1 clusters in both endogenous (26, 29, 31–35) and heterologous systems (20, 27, 30, 33, 56). Using 3D-MINFLUX/DNA-PAINT nanoscopy, we corroborate and expand upon these findings by showing that most PIEZO1 clusters form pit-shaped invaginations in the plasma membrane (Fig. 5, C to K). The interpretation that these invaginations

are contiguous with the plasma membrane rather than intracellular vesicular structures is supported by the observation that Yoda2-induced Ca^{2+} signals originating from PIEZO1 clusters require extracellular calcium (Fig. 4G) and by our extracellular ALFA-tag labeling experiments (Fig. 4, C to E). Moreover, we found that mechanical stimulation via hypoosmotic stress caused significant flattening of these pit-like structures and Gaussian curvature mapping revealed a redistribution of PIEZO1 channels within the pits upon hypoosmotic challenge such that more channels are exposed to convex curvature (Fig. 7), a condition previously shown to facilitate channel opening (8, 72). PIEZO1 pits come in various depths as evident from relatively large SD of depth measurements, which together with the large sample size call for caution when interpreting statistical significances. Nevertheless, it is tempting to speculate that the curvature gradient along the pit axis offers an energetically favorable microenvironment for mechanotransduction, where small changes in pit shape could alter the local mechanical landscape experienced by individual channels.

With regard to the effect of clustering on PIEZO1 structure and function, *in silico* modeling studies had suggested that the opposing curvatures of the membrane footprints of two nearby channels would create an energetic constraint in the interjacent membrane such that nearby channels would either repel each other or induce mutual flattening to reduce the overall energy of the system (6, 12, 39). Our data contradict these models and demonstrate that clustering instead causes the formation of pit-shaped invaginations that accommodate up to twenty channels and more (Fig. 5). PIEZO1 appears to prefer concave membrane environments as it was shown to accumulate in the dimple region of red blood cells (36), cardiomyocyte T-tubules (32), and artificially induced membrane curvatures (59), which raised the question whether the PIEZO1-pits observed here resulted from the accumulation of PIEZO1 in preexisting invaginations or whether PIEZO1 itself actively contributed to their formation. The lack of colocalization of PIEZO1 with clathrin, Cav1, and COP1 together with the insensitivity of cluster density to pharmacological inhibition of clathrin-mediated endocytosis (Fig. 6, A and B) demonstrate that PIEZO1 pits are distinct from classical membrane invaginations such as clathrin-coated pits, caveolae, or COP1-associated vesicles, which supports the latter idea. Moreover, cluster formation was not altered by inhibition of traction forces with blebbistatin, disruption of the cytoskeleton by cyto-D, and in cells lacking Stoml3 (Fig. 6C). Considering that PIEZO1 exerts a strong bending force onto membranes (7, 8, 11), pit formation appears to be an effective mechanism to minimize the energy of the PIEZO1 cluster system, by allowing the membrane footprints of individual PIEZOs to seamlessly integrate into the overall pit curvature without causing energetic constraints in the membrane between neighboring channels PIEZOs. Thus, although we cannot definitively rule out a contribution of other, yet unidentified, membrane bending proteins, it is tempting to speculate that PIEZO1 itself might actively drive pit formation—a hypothesis that is further fuelled by the intriguing structural resemblance of PIEZO1 with the well-described coat proteins clathrin and COP1 (Fig. 6D), which are well-known to sculpt membrane pits.

Collectively, our findings suggest a model in which PIEZO1 clusters are not passive aggregates but rather functionally and structurally specialized units that create distinct microenvironments within the plasma membrane. These clusters may act as localized mechano-responsive microdomains capable of amplifying mechanical stimuli via structural changes in their topology. Thus, our work provides a framework for future studies that should address the molecular

determinants of cluster formation, the role of lipid microdomains in organizing these structures, and whether accessory proteins contribute to the formation and stabilization of pit-shaped PIEZO1 clusters.

MATERIALS AND METHODS

Generation of PIEZO constructs

A mouse PIEZO1–internal ribosomal entry site (IRES)–green fluorescent protein (GFP) plasmid (Addgene, #80925) was used as the initial template to generate most of the constructs of the present work, using a similar strategy described in earlier studies (20, 56). PIEZO1–mGreenLantern fusion protein (PIEZO1–mGL) was generated by amplifying the coding sequence of the GFP mGreenLantern (73) from a LifeAct–mGreenLantern plasmid (gift from G. Petsko, Addgene, #164459), and inserted with an SG linker after the C-ter of the PIEZO1 plasmid, where the IRES–GFP sequence has been excised beforehand by polymerase chain reaction (PCR). PIEZO1–mScarlet was generated with restriction enzymes, by digesting the PIEZO1–IRES–GFP plasmid with BspEI and FseI enzymes (New England Biolabs) and a PCR-amplified mScarlet fragment from a pAAV–CAG–FLEX–mScarlet plasmid (gift from R. Larsen, Addgene, #99280) and ligation (T4 ligase, Promega) was performed overnight at 16°C. The PIEZO1–ALFA–IRES–GFP construct was generated by inserting a synthetic DNA fragment coding for amino acid 1 to 180 of mouse PIEZO1, with the ALFA-tag sequence inserted after amino acid position H86 and flanked by one proline on each side (GeneArt Custom Gene Synthesis, Thermo Fisher Scientific) (74), into a PIEZO1–IRES–GFP plasmid excised by PCR for the corresponding 1 to 180 coding region. A plasmid version of PIEZO1–ALFA without the IRES–GFP sequence but with a C-ter hemagglutinin (HA) tag was also generated using a previously generated PIEZO1–HA template (75). The PIEZO1–ALFA–IRES–GFP plasmid was later used as a template to generate the PIEZO1–ALFA–mGreenLantern (PIEZO1–ALFA–mGL) by exchanging the IRES–GFP sequence with mGreenLantern, as described above. The PIEZO1–jGCaMP8m fusion was generated by inserting at the C-ter of PIEZO1 the coding sequence of jGCaMP8m (76) (a gift from GENIE Project, Addgene, #162372) with a GSGG linker, following a similar and validated strategy described previously (38). To facilitate visualization of transfected cells due to the low basal fluorescence of the jGCaMP8m fusion, a second plasmid was generated by adding a P2A–mScarlet sequence after the jGCaMP8m. All DNA fragments were generated by PCR (primers from Sigma–Aldrich) using KAPA HiFi polymerase (Roche), and cloning was performed with homologous recombination (Gibson Assembly, NEBuilder HiFi, New England Biolabs). PCR reactions were digested with DpnI (New England Biolabs, 37°C, 1 hour) and column purified with standard kits (NucleoSpin from Macherey–Nagel or PureLink from Invitrogen) before being assembled by homologous recombination and then transformed in electrocompetent Stb14 or Dh5a bacteria (Invitrogen) and grown at 30°C for 48 hours (Stb14) or 37°C overnight (Dh5a). Selected clones were entirely sequenced (Eurofins) to ensure that no mutation was present.

Generation of N2a–Stoml3–KO cells

A genomic deletion of the *STOML3* gene locus in N2A cells was introduced using CRISPR–Cas9 gene targeting (77). Guide sequences were designed so that a complete deletion of Exon 1 of the *Stoml3* gene was achieved in several independent clones. Eight clones were selected, and the genomic deletion verified by sequencing fragments

amplified from the targeted region (fig. S6D). The deletion introduced a frameshift to abolish expression of the full-length *STOML3*. One clone was selected for functional analysis using electrophysiology to measure indentation-evoked currents as described (fig. S6, E and F) (78).

Cell culture

Mouse neuroblastoma Neuro-2a PIEZO1–KO cell line (N2A–PIKO) was generated and characterized previously from Neuro-2a American Type Culture Collection (ATCC) CCL-131 [a gift from G. R. Lewin (43)]. Cells were grown in Dulbecco's modified Eagle's medium (DMEM) and optimal minimal essential medium (1:1 mixture), supplemented with 10% fetal bovine serum (FBS), 2 mM L-glutamine, and 1% penicillin–streptomycin (all from Thermo Fisher Scientific). U87 (U87–MG, ATCC HTB-14) and MEF (ATCC SCRC-1008) were grown in DMEM supplemented with 10% FBS and 1% penicillin–streptomycin. For some live TIRF imaging experiments, medium without phenol red was used. Cells were cultured at 37°C with 5% CO₂. Cells were seeded on PLL (Sigma–Aldrich)–coated and methanol- and acid-washed glass coverslips (12-mm diameter for patch-clamp recordings, #1.5 and 18-mm diameter for Minflux and TIRF imaging on fixed samples), or PLL-coated 35-mm glass-bottom dishes (MatTek High Precision #1.5 Coverslip, TIRF microscopy live imaging). Cells were transfected 1 or 2 days after plating using polyethylenimine (PEI, Linear PEI 25 K, Polysciences). For one 12-mm coverslip, 7 μ l of a PEI solution (360 μ g/ml) is mixed with 9 μ l of phosphate-buffered saline (PBS). Plasmid DNA is diluted in 20 μ l of PBS (0.6 μ g per coverslip), and then, the 16- μ l PEI–PBS solution is added to the DNA solution. After at least 10 min of incubation at room temperature, the DNA–PEI mix is added drop by drop and mixed by gentle swirling. For a 35-mm dish or 18-mm coverslip, 2.0 μ g DNA is used and PBS/PEI volumes are adjusted accordingly. Twenty-four hours later, the medium is replaced by a fresh one. In selected experiments investigating neurites, N2A–PIKO cells were serum-starved for approximately 12 hours to promote neurite outgrowth. Cells were then used within 24 to 48 hours.

Electrophysiology

All PIEZO constructs generated were tested for proper functionality in patch-clamp assays and compared to control PIEZO1–IRES–GFP. Mechanically activated currents were recorded at room temperature using EPC10 amplifier with Patchmaster software (HEKA Elektronik). Borosilicate patch pipettes (2 to 6 megohm for whole cell and 1.5 to 3.5 megohm after fire-polishing for cell-attach) were pulled with a P-97 Flaming–Brown puller (Sutter Instrument). For whole-cell patch clamp, intracellular buffer contained the following: 125 mM K-gluconate, 7 mM KCl, 1 mM MgCl₂, 1 mM CaCl₂, 4 mM EGTA, and 10 mM Hepes (pH 7.3 with KOH) and for single-channel cell-attach, 130 mM NaCl, 5 mM KCl, 1 mM MgCl₂, 1 mM CaCl₂, 10 mM Hepes, 10 mM TEA–Cl (pH 7.3 with NaOH). The control bath solution for whole-cell contained the following: 140 mM NaCl, 4 mM KCl, 1 mM MgCl₂, 2 mM CaCl₂, 4 mM glucose, and 10 mM Hepes (pH 7.4 with NaOH). For single channel recordings, the bath solution contained: 140 mM KCl, 1 mM MgCl₂, 2 CaCl₂, 10 glucose, and 10 mM Hepes (pH 7.4 with KOH). Cells were held at a holding potential of –60 mV (whole-cell and cell-attach).

Mechanical stimulation in whole-cell experiments was done with a series of 15 mechanical stimuli in 0.6- μ m increments with a fire-polished glass pipette (tip diameter, 2 to 3 μ m) that was positioned

opposite to the recording pipette, at an angle of approximately 45° to the surface of the dish and moved with a velocity of 1 $\mu\text{m}/\text{ms}$ by a piezo-driven micromanipulator (Preloaded Piezo actuator P-840.20, Physik Instrumente). Negative pressure stimuli in cell-attach experiments were applied for 500 ms with the High-Speed Pressure Clamp device (ALA Scientific Instruments), with -5 mmHg increments up to 80 mmHg. A pre-pulse of $+5$ mmHg was applied before negative-pressure stimuli to improve recovery from inactivation (72). For current-voltage relation (I/V) experiments, pressure stimulus was adjusted on a cell-by-cell basis to optimally evoke single-channel openings.

The evoked whole-cell currents were recorded with a sampling frequency of 200 kHz and filtered with 2.9-kHz low-pass filter. Pipette and membrane capacitance were compensated using the auto function of Patchmaster. Recordings with excessive leak currents, unstable access resistance, and cells that giga-seals did not withstand at least seven consecutive mechanical steps stimulation were excluded from analyses. Mechanical thresholds of PIEZO currents were determined by measuring the mechanical stimulus that evoked the first sizeable peak current, defined as the point in which the current significantly differed from the baseline (more than six times the SD of the baseline). The inactivation time constants (τ_{inact}) were measured by fitting the mechanically activated currents with a single exponential function $\{C1 + C2 * e^{-[(t-t_0)/\tau_{\text{inact}}]}\}$, where C1 and C2 are constants, t is time, and τ_{inact} is the inactivation time constant. For each cell, only peak currents between 100 and 1500 pA were used for τ_{inact} calculation and averaged from cell to cell.

The evoked cell-attach currents were recorded with a sampling frequency of 50 kHz and filter with a 2.9-kHz low-pass filter. Maximal pressure-evoked currents over the course of a given stimulus (I) were normalized to the absolute maximal response of the cell at any pressure (I_{max}). Normalized pressure-response curve (I/I_{max}) from individual cells were fitted with a Boltzmann sigmoid to determine individual P50 (in mmHg).

Single-channel amplitudes at a given holding potential (-140 to -40 mV, 20-mV steps) were determined as the difference between the peaks of the Gaussian fits of the trace histogram over multiple 1-s segments. Unitary conductance was determined from the linear regression fits of the I/V plot of individual cells. Recordings with excessive leak currents or unstable baseline were excluded. Recordings that displayed noninactivating responses or unstable openings were also not used for further I/V analyses. All electrophysiology analysis was performed in IgorPro (Wavemetrics) using custom scripts.

Calcium imaging of neurites

N2A-P1KO cells were plated on 12-mm coverslips, transfected with PIEZO1-mScarlet (0.6 μg per coverslip) together with a CMV-jGCaMP8m vector (0.2 μg per coverslip) and serum starved to promote neurite outgrowth. For control experiments (ionomycin), only jGCaMP8m was transfected. Cells were washed once with PBS and incubated with a calcium imaging buffer containing 140 mM NaCl, 4 mM KCl, 1 mM MgCl_2 , 3 mM CaCl_2 , 4 mM glucose, and 10 mM Hepes (pH 7.4 with NaOH). Fluorescent images were acquired every second (500-ms exposure time, Yoda1 experiments) or every 5 s (1-s exposure time, ionomycin experiments) on an Olympus BX40 upright microscope equipped with standard Quad filter (Chroma), fluorescent lamp (HBO 100) and shutter (Lambda 10-2, Sutter Instrument) with a 40 \times water-immersion objective (LUMPlanFI/IR, Olympus), visualized with a CoolSnap HQ2 camera (Photometrics) and acquired with the MetaFluor software (Molecular Devices).

Perfusion and fast solution exchanged was achieved with a gravity-driven perfusion system (ValveLink8.2, AutoMate Scientific). Cells were first perfused with control solution for at least 20 s before being exposed to Yoda1 (Sigma-Aldrich, 100 nM, 300 nM, or 1 μM) for 20 s, followed with a washout with control solution. For ionomycin control experiments (Tocris), cells were perfused with control solution and then exposed to ionomycin (10 μM), first in an imaging buffer without CaCl_2 but with 5 mM EDTA (0 calcium) and then to one containing increasing CaCl_2 concentration (100 μM , 300 μM , 1 mM, 3 mM, 10 mM calcium) for 5 min for each concentration. Ionomycin was kept in the buffers throughout the recording. Only one field of view per coverslip was used to avoid Yoda1 or ionomycin leakage. Only cells that are double positive for PIEZO1 and jGCaMP8m and that have neurites were considered for analysis. Cell body and associated neurites were segmented in ImageJ, and the time course of normalized fluorescence ratio (F/F_0) was calculated as the ratio between the jGCaMP8m fluorescence intensity [arbitrary unit (a.u.)] at a given time (F) and the average fluorescence intensity per PIEZO-mScarlet transfected cell averaged over a 10-s interval during the initial control perfusion (F_0). Within a given Yoda1 or ionomycin concentration perfusion time, the maximal F/F_0 ratio per cell was extracted. For a cell having multiple neurites, values were averaged and ultimately compared to its cell body with paired test.

Preparation of samples for TIRF imaging

For live samples, N2A-P1KO cells were plated on glass-bottom dishes as described before and transfected with PIEZO1-ALFA-mGL (live labeling) or PIEZO1-jGCaMP8m (calcium imaging of PIEZO clusters). Two to three days after transfection, the samples were processed for live labeling and imaging. For live labeling, the cells were washed once with phenol-red-free medium and incubated for 3 min at 37°C with a nanobody against ALFA tag conjugated to Alexa Fluor 647 (FluoTag-X2 anti-ALFA, NanoTag Biotechnologies, RRID: AB_3075981) diluted 1:100 in cell culture medium. The cells were then washed twice and imaged immediately. Labeled live samples were kept for no more than 20 min. To evaluate the impact of clathrin-mediated endocytosis on the number of PIEZO clusters in living cell, the dynamin inhibitor Dynasore (Sigma-Aldrich; final concentration, 75 μM) was preincubated for 2 hours before and kept during the image acquisition. For calcium imaging, the cells were incubated in a buffer containing 140 mM NaCl, 4 mM KCl, 1 mM MgCl_2 , 3 mM CaCl_2 , 4 mM glucose, and 10 mM Hepes (pH 7.4 with NaOH) and then perfused for 20 s with a 2.5 μM solution of Yoda2 (Sigma-Aldrich). In experiments with no extracellular calcium, the 3 mM CaCl_2 were replaced by 5 mM EDTA.

For fixed samples, N2A-P1KO, U87, or MEF cells were plated on 18-mm coverslips. In experiments investigating accessibility of PIEZO cluster, N2A-P1KO cells were transfected with PIEZO1-ALFA-mGL. In experiments investigating PIEZO cluster and their colocalization with different markers, N2A-P1KO, U87, and MEF cells were transfected with PIEZO1mScarlet or PIEZO1mScarlet together with a plasmid encoding Clathrin Light Chain fused to mGL (Clc-mGL, gift from G. Petsko, Addgene, #164462) to visualize clathrin coated pits. In some experiments, N2A-P1KO without PIEZO1 transfected were used to evaluate its potential impact on invagination formation. In experiments investigating native PIEZO1 clusters in MEF and U87, the cells were not transfected. Two to three days after transfection or plating (native PIEZO1 clusters), cells were washed once with PBS and fixed for 10 min at room temperature with a mixture

of 1% paraformaldehyde (PFA) and 0.1% glutaraldehyde in PBS. Fixative was removed and quenched with 5 mM NaBH₄ in PBS (one quick wash and another one for 5 min at room temperature) and then with 50 mM glycine and 50 mM NH₄Cl in PBS (one quick wash and another one for 5 min at room temperature). Samples were further washed thrice with PBS for 5 min at room temperature. In experiments evaluating accessibility of PIEZO clusters in N2A-PIKO, cells were then blocked with either a mix of 5% FBS plus 1% BSA in PBS (no permeabilization) or with additionally 0.2% Triton 100-X and 0.05% Tween 20 (permeabilization) for 30 min at room temperature. Samples were then labeled with the ALFA nanobody conjugated to Alexa Fluor 647 diluted 1:100 into respective blocking buffers and incubated for 1 hour at room temperature. For colabeling experiments and exploration of native PIEZO1 clusters, the cells were processed with the permeabilized buffer and then incubated overnight at 4°C with either a rabbit antibody against Cav1 (1:200) (Abcam, RRID: A_B_303405), a rabbit antibody against COPI α (1:1000) (Thermo Fisher Scientific, 23GB3485, RRID: AB_3249045), or a rabbit antibody against PIEZO1 (1:100) (Novus NBP1-78446, RRID: AB_11020328) diluted in permeabilized buffer. Samples were then washed three times for 5 min at room temperature with their respective blocking buffers. A postfixation step was performed for ALFA nanobodies, using the same fixative mixture as before, for 5 min. Fixatives were quenched and then washed three more times with PBS. For colabeling or native PIEZO1 labeling, samples were incubated for 1 hour at room temperature with a donkey anti-rabbit antibody coupled to Alexa Fluor 647 (1:1000) (Life Technologies). After several washes, coverslips were then mounted on slides with ProLong Glass Antifade Mountant (Thermo Fisher Scientific). Samples were then imaged within 2 days.

TIRF microscopy imaging and acquisition

TIRF imaging was performed on a Nikon Eclipse TiE microscope and with a Roper iLAS2 TIRF module. The objective was an oil immersion Nikon CFI Plan Apo Lambda 100 \times (numerical aperture, 1.45), and the camera used was a Photometrics Prime 95B back-illuminated sCMOS, having a resolution of 1200 \times 1200 and with a pixel size of 11 μ m, giving a final pixel size of 0.110 μ m. A 1.5 \times magnification lens was added for some experiments, giving a final pixel size of 0.073 μ m. Cells were illuminated with solid-state lasers of 488, 560, and 640 nm (20% power). Acquisition was done with VisiView software (version 5.0.0, Visitron Systems). For live imaging, an incubation chamber (okolab) was used to adjust temperature (37°C), CO₂-concentration (5%) and humidity. Live cells were imaged for 30 s with a frame rate of 10 Hz (approximately 100-ms exposure time per frame) for live labeling experiments, or for 2 min with a frame rate of 2 Hz (calcium imaging).

TIRF microscopy analysis

Because of the mobility of PIEZO clusters in live cell, clusters were tracked for analysis as described before (20, 56). For calcium imaging experiments, time-lapse recordings were first preprocessed in ImageJ with a bleach correction [simple ratio, (79)]. PIEZO track analysis was then performed with TrackMate v7.13.2 (80, 81) and the following parameters: DoG detector, blob diameter of 0.35 μ m, spots quality filter value of 0.10 to 1, simple LAP tracker with a linking distance of 0.7 μ m, a gap closing distance of 0.7 μ m, and a maximal gap closing frame number of 2. The average intensity over time within each detected cluster was then extracted and normalized to

the baseline, defined as the average intensity over the last 10 s of acquisition before Yoda2 was applied. For live labeling experiments, clusters were detected and counted in the first frame with TrackMate using the same parameters as above.

For fixed samples and experiments investigating the extracellular accessibility of the cluster, analysis was performed in ImageJ. PIEZO clusters were identified on the mGL signal (488-nm excitation): A background subtraction (rolling ball radius 5) was first performed, a Gaussian blur was applied (sigma 2 and 3), and blurred images were subtracted. An auto-local threshold was then used (Bernsen method, radius 5) followed by a particle detection (min. size = 10 and max. size = 50 pixels) to identify clusters as regions of interest (ROIs). Intensity of the mGL and ALFA-Alexa Fluor 647 signals were then measured within the ROIs and mGL clusters were classified or not as ALFA-Alexa Fluor 647 positive. A similar approach was used to investigate colocalization of PIEZO1mScarlet cluster with the selected cellular markers. For fixed samples and experiments investigating endogenous PIEZO1 clusters and their size (Fig. 1), clusters were detected with TrackMate as ROIs and their coordinates were extracted, imported in IgorPro and fitted with a 2D Gaussian fit to estimate their diameter.

Preparation of samples for DNA-PAINT MINFLUX imaging

N2A-PIKO cells were plated on 18-mm coverslips as described in previous section and transfected with PIEZO1-mGL, PIEZO1-ALFA-HA, or PIEZO1-ALFA-mGL. N2A-SLP3KO were used for some experiments and transfected with PIEZO1-ALFA-mGL. Two to three days after transfection, cells were processed for fixation as described above for TIRF imaging or first serum starved, treated with hypotonic solution, Yoda1 or cyto-D, and then fixed as described above. For hypoosmotic experiments, cells were washed once with PBS and then incubated for 3 min at 37°C in a 120-mosmol Ringer's solution [48.8 mM NaCl, 5 mM KCl, 10 mM Hepes, and 10 mM glucose (pH 7.4)] and finally fixed for at least 15 min at room temperature in a hypotonic fixative (0.5% PFA and 0.05% glutaraldehyde, 200 mosmol). For cyto-D (Sigma-Aldrich) experiments, cells were incubated for 20 min at 37°C with 2 μ M cyto-D diluted in culture medium, which was kept after in the fixative solution (Minflux imaging) or in the extracellular buffer (electrophysiology). For blebbistatin experiments (Tocris), cells were incubated for 1 hour at 37°C with 30 μ M blebbistatin diluted in culture medium, which was kept after in the fixative solution. For Yoda1 experiments, cells were incubated for 3 min at 37°C with 50 μ M Yoda1 diluted in culture medium, which was kept after in the fixative solution. After quenching and washing of fixatives, samples were blocked with antibody incubation buffer (Massive Photonics) for 30 min at room temperature. The cells were incubated for 1 hour at room temperature or overnight at 4°C with Massive-Tag-Q anti-ALFA or anti-GFP nanobodies conjugated with a DNA docking strand (both from Massive Photonics) diluted at 1:100 (anti-ALFA) or 1:200 (anti-GFP) in antibody incubation buffer. PIEZO1-ALFA-HA samples were fixed, blocked, and permeabilized as described above for TIRF samples and then incubated with the anti-GFP nanobody and with a rabbit anti-HA antibody (1:500, Thermo Fisher Scientific, RRID: AB_2533988). Cells were washed thrice with 1 \times washing buffer (Massive Photonics) and then post-fixed for 5 min. Fixatives were quenched and washed as described before. PIEZO1-ALFA-HA samples were then incubated for 1 hour at room temperature with a secondary antibody donkey anti-rabbit coupled to Alexa Fluor 488 (1:1000) (Life technologies) and further

washed with PBS. Samples were then incubated for 10 min with 100 to 200 μl of gold nanoparticles for future stabilization (gold colloid 250 nm, BBI Solutions, or A12-40-980-CTAB, Nanopartz). Unbound nanoparticles were rinsed extensively with PBS, and the remaining nanoparticles were further stabilized with PLL for at least 1 hour at room temperature. Cells were then washed thrice with PBS before mounting. Labeled samples were used within 3 days. DNA-PAINT imagers (Massive Photonics) conjugated to Atto 655 were freshly diluted in Imaging buffer (Massive Photonics) for a final concentration of 1 to 2 nM (Atto 655 and ALFA imaging, Imager sequence #3) or 1 nM (Atto655 and GFP imaging, Imager sequence #2). A drop of imager dilution was added into a cavity slide, and coverslips were mounted and sealed with picodent twinsil (picodent).

3D MINFLUX imaging

Minflux imaging was performed on an Abberior MINFLUX commercial microscope built on an inverted IX83 microscope with a 100 \times UPlanXApo objective (Olympus) and using Inspector Software (Abberior Instruments). Daily alignment and calibration of the excitation beam pattern and position of the pinhole was performed using fluorescent nanoparticles (Abberior Nanoparticles, Gold 150 nm, 2C Fluor 120 nm, Abberior Instruments). Cells were identified with a 488-nm confocal scan, and the transient binding of imagers with Atto 655 was quickly verified with 640-nm confocal scan. At least two gold fiducials were present in the field of view and used by the active-feedback stabilization system of the microscope (IR 975-nm laser, Cobolt, and CCD camera, The Imaging Source), having typically a precision below 1 nm in all three axes and being stable for hours. An ROI of 1 μm by 1 μm to 5 μm by 5 μm (up to 8 μm by 8 μm for some overnight recordings) was selected at the cell-coverslip interface, except for some neurites where focus was set approximately in their middle height. Laser power in the first iteration and pinhole was set at 16% laser power and 0.83 A.U. pinhole. Final laser power in the last iteration is scaled up by a factor of 6. ROIs were imaged for at least 2 hours and up to overnight (~12 hours) using the standard 3D Minflux sequence (table S1). Detection for Atto 655 signals was performed with two avalanche photodiodes channels (650 to 685 nm and 685 to 720 nm) that were pooled. Specificity of the nanobodies and imagers used in this study and of the Minflux signal was tested by incubating samples transfected with PIEZO1-mGL with the anti-ALFA nanobody and samples transfected with PIEZO1-ALFA-HA with the anti-GFP nanobody (figs. S2D and S7C).

MINFLUX data analysis

Final valid localizations from Minflux iterations were exported from Inspector software as Matlab files. Custom Matlab scripts were then used for postprocessing and filtering of the data, as well as subsequent operations and data visualization. Data filtering involved first an efo filter (effective frequency at offset, kilohertz, retrieved for each individual valid locations) based on its overall distribution for each individual measurements: a threshold was then selected to filter-out potential multiple emitters. An additional cfr filter (center frequency ratio) was used for mGL/GFP cluster experiments, with a cutoff value of 0.5 (0.8 elsewhere, directly implemented during the acquisition). Then, localizations from the same emission trace, i.e., with the same trace identification number (TID), having an SD of more than 10 nm in the x , y , z axes and less than three (ALFA) or five (GFP) localizations were excluded (see fig. S2D). For ALFA signals, filtered traces were trimmed of their first two localizations, as they are often

apart from the rest and most of the localization cloud possibly caused by diffusing imager molecules. For GFP signals, in addition to trimming, localizations for each trace were aggregated (group of three), as described elsewhere (82). The remaining traces were further corrected for the refractive index mismatch between the coverslip and the sample, applying a scaling factor of 0.7 for all traces in the z dimension (40).

For mGL/GFP cluster experiments (Figs. 5 and 6), clusters were semimanually selected on the basis of a first-round DBSCAN (variable parameters adjusted with imaging signal density, typically epsilon of 80 to 160 nm and minPoints of 100 raw localizations) and analyzed as follows. The center of mass of each individual filtered trace (i.e., trace with the same TID) within the clusters was calculated. Because of the nature of DNA-PAINT labeling and the proximity of individual mGL molecules at PIEZO C-ter, neighboring signals coming from the same PIEZO channel were estimated and averaged using a DBSCAN on the trace average calculated before, with a minPoints of 2 and epsilon of 25 nm (based on recording precision and labeling error), ultimately giving a position of an individual PIEZO channel (see fig. S7). To classify clusters into pit-shaped (open at the top) and spherical clusters, we segmented the raw MINFLUX localization data of each cluster into signals originating from the upper fifth (top) and the lower four-fifth (bottom) (Fig. 5F) and classified clusters in which no channels were present near the center of the top segment (i.e., within a distance of 0.25 times the radius from the centroid), as pit-shaped clusters, whereas those clusters that did contain channels in this region were considered as spherical clusters (Fig. 5G). To estimate the local curvature of the membrane at the position of individual PIEZO1 channels within cluster, we fitted the 3D distribution of the traces mean making the cluster using a modified 2D Gaussian distribution that contained a term correcting for cluster width, $Z = \text{top} + \text{depth} - \text{depth} / [1 + e^{\{2 \cdot \text{width}^2 - [(X - \text{CenterX})^2] - [(Y - \text{CenterY})^2]\} / \text{slope}^2}]$, where X , Y , and Z are the coordinates of the channels, CenterX and CenterY are the arithmetic means of the X and Y coordinates of all channels. For surface fitting “top” (Z coordinate of the topmost channel) and “depth” (distance between the topmost and the lowest channel) were held constant and the width and slope of the clusters were fitted using the custom fit function in IgorPro. Fitting was performed using the Levenberg-Marquardt least orthogonal distance method implemented in IgorPro8 (wavemetric) that is based on the ODRPACK95 code (83). The Gaussian curvatures at the coordinates of the channels were then calculated using a custom written script in Matlab (see code availability).

For ALFA trimer experiments, signals were filtered and the center of mass of each individual trace was calculated. Traces originating from repeated detection of the same protomer were identified using DBSCAN clustering with minPoints of 2 and epsilon of 8 nm. The 8-nm cutoff was chosen on the basis of the localization precision of MINFLUX and the possible ALFA-tag flexibility (Fig. 1B). The position of the protomers that were detected multiple times was determined by calculating the mean coordinate of the localizations clustered by the DBSCAN algorithm. PIEZO1 trimers in which all three protomers were labeled and detected by MINFLUX were identified by searching for three adjacent traces that were less than 40 nm apart, which we assumed is the maximum distance two Atto 655 molecules bound to the same PIEZO1 trimer can possibly have based on available flattened PIEZO1 structures and that had no other neighboring traces within a distance of 60 nm (fig. S3). Moreover, only trimers in which the maximum interblade angle was smaller than

120° were considered. Interblade distance for a given trimer was calculated as the average of the three protomers distance. Interblade distance distribution was fitted with a Gaussian mixture model in Matlab. Further visualization of trimers was done by a 2D in-plane projection of the raw localizations for each protomer, followed by a fit with a bivariate Gaussian distribution and displayed with its probability density.

Structure modeling and data visualization

For visualization purposes, full-length PIEZO1 in different putative conformations were generated. The predicted AlphaFold structure of mouse PIEZO1 (AF-E2JF22-F1-v4) was aligned and superposed onto the experimentally determined curved [Protein Data Bank (PDB) 6B3R], flat (PDB 7WLU), and intermediate-flat (PDB 8IXO) PIEZO1 structure to visualize the unresolved peripheral blade. The final constructs display the experimentally resolved structure with the added missing blade parts from AlphaFold as transparent color (Fig. 1H). A full-length PIEZO1 trimer bearing an ALFA tag at position H86 and a C-ter GFP together with their respective nanobody (PDB 6I2G for ALFA, PDB 3K1K for mGL/GFP), DNA docking site, imager and fluorophore was also generated. All subsequent modification operations and visualization were performed in PyMol (version 2.5.5, Schrödinger). Plasmid design and visualization was performed with SnapGene (version 7, Dotmatics). All the other data, graphics and schematics were elaborated and visualized in Matlab, IgorPro, Illustrator (Adobe), and GraphPad Prism (version 10, GraphPad Software).

Statistical tests and reproducibility

All experiments in this study were performed independently at least three times, yielding similar results. No statistical method was used to predetermine sample size. Experiments were not randomized, and investigators were not blinded during experiments and analysis. Data distribution was systematically evaluated using D'Agostino–Pearson test and parametric or nonparametric tests were chosen accordingly. The statistical tests that were used, the exact *P* values, and information about the number of replicates are provided in the display items or the corresponding figure legends.

Supplementary Materials

The PDF file includes:

Figs. S1 to S11

Table S1

Legends for movies S1 to S7

Other Supplementary Material for this manuscript includes the following:

Movies S1 to S7

REFERENCES AND NOTES

- M. Szczot, A. R. Nickolls, R. M. Lam, A. T. Chesler, The form and function of PIEZO2. *Annu. Rev. Biochem.* **90**, 507–534 (2021).
- J. Wu, A. H. Lewis, J. Grandl, Touch, tension, and transduction – The function and regulation of piezo ion channels. *Trends Biochem. Sci.* **42**, 57–71 (2017).
- B. Xiao, Mechanisms of mechanotransduction and physiological roles of PIEZO channels. *Nat. Rev. Mol. Cell Biol.* **25**, 886–903 (2024).
- J. M. Kefauver, A. B. Ward, A. Patapoutian, Discoveries in structure and physiology of mechanically activated ion channels. *Nature* **587**, 567–576 (2020).
- P. Ridone, M. Vassalli, B. Martinac, Piezo1 mechanosensitive channels: What are they and why are they important. *Biophys. Rev.* **11**, 795–805 (2019).
- M. Young, A. H. Lewis, J. Grandl, Physics of mechanotransduction by Piezo ion channels. *J. Gen. Physiol.* **154**, e202113044 (2022).
- X. Yang, C. Lin, X. Chen, S. Li, X. Li, B. Xiao, Structure deformation and curvature sensing of PIEZO1 in lipid membranes. *Nature* **604**, 377–383 (2022).
- Y.-C. Lin, Y. R. Guo, A. Miyagi, J. Levring, R. MacKinnon, S. Scheuring, Force-induced conformational changes in PIEZO1. *Nature* **573**, 230–234 (2019).
- A. H. Lewis, J. Grandl, Inactivation kinetics and mechanical gating of Piezo1 ion channels depend on subdomains within the cap. *Cell Rep.* **30**, 870–880.e2 (2020).
- Y. Wang, S. Chi, H. Guo, G. Li, L. Wang, Q. Zhao, Y. Rao, L. Zu, W. He, B. Xiao, A lever-like transduction pathway for long-distance chemical- and mechano-gating of the mechanosensitive Piezo1 channel. *Nat. Commun.* **9**, 1300 (2018).
- C. A. Haselwandter, Y. R. Guo, Z. Fu, R. MacKinnon, Quantitative prediction and measurement of Piezo's membrane footprint. *Proc. Natl. Acad. Sci. U.S.A.* **119**, e2208027119 (2022).
- C. A. Haselwandter, R. MacKinnon, Piezo's membrane footprint and its contribution to mechanosensitivity. *eLife* **7**, e41968 (2018).
- C. Verkest, S. G. Lechner, Advances and recent insights into the gating mechanisms of the mechanically activated ion channels PIEZO1 and PIEZO2. *Curr. Opin. Physiol.* **31**, 100625 (2023).
- S. Liu, X. Yang, X. Chen, X. Zhang, J. Jiang, J. Yuan, W. Liu, L. Wang, H. Zhou, K. Wu, B. Tian, X. Li, B. Xiao, An intermediate open structure reveals the gating transition of the mechanically activated PIEZO1 channel. *Neuron* **113**, 590–604.e6 (2025).
- Y. R. Guo, R. MacKinnon, Structure-based membrane dome mechanism for Piezo mechanosensitivity. *eLife* **6**, e33660 (2017).
- K. Saotome, S. E. Murthy, J. M. Kefauver, T. Whitwam, A. Patapoutian, A. B. Ward, Structure of the mechanically activated ion channel Piezo1. *Nature* **554**, 481–486 (2018).
- Q. Zhao, H. Zhou, S. Chi, Y. Wang, J. Wang, J. Geng, K. Wu, W. Liu, T. Zhang, M.-Q. Dong, J. Wang, X. Li, B. Xiao, Structure and mechanogating mechanism of the Piezo1 channel. *Nature* **554**, 487–492 (2018).
- P. A. Gottlieb, C. Bae, F. Sachs, Gating the mechanical channel Piezo1: A comparison between whole-cell and patch recording. *Channels (Austin)* **6**, 282–289 (2012).
- C. D. Cox, C. Bae, L. Ziegler, S. Hartley, V. Nikolova-Krstevska, P. R. Rohde, C.-A. Ng, F. Sachs, P. A. Gottlieb, B. Martinac, Removal of the mechanoprotective influence of the cytoskeleton reveals PIEZO1 is gated by bilayer tension. *Nat. Commun.* **7**, 10366 (2016).
- C. Verkest, I. Schaefer, T. A. Nees, N. Wang, J. M. Jegelka, F. J. Taberner, S. G. Lechner, Intrinsically disordered intracellular domains control key features of the mechanically-gated ion channel PIEZO2. *Nat. Commun.* **13**, 1365 (2022).
- H. J. Wang, Y. Wang, S. S. Mirjavadi, T. Andersen, L. Moldovan, P. Vatanekha, B. Russell, J. Jin, Z. Zhou, Q. Li, C. D. Cox, Q. P. Su, L. A. Ju, Microscale geometrical modulation of PIEZO1 mediated mechanosensing through cytoskeletal redistribution. *Nat. Commun.* **15**, 5521 (2024).
- J. Wang, J. Jiang, X. Yang, G. Zhou, L. Wang, B. Xiao, Tethering Piezo channels to the actin cytoskeleton for mechanogating via the cadherin- β -catenin mechanotransduction complex. *Cell Rep.* **38**, 110342 (2022).
- E. M. Mulhall, A. Gharpure, R. M. Lee, A. E. Dubin, J. S. Aaron, K. L. Marshall, K. R. Spencer, M. A. Reiche, S. C. Henderson, T.-L. Chew, A. Patapoutian, Direct observation of the conformational states of PIEZO1. *Nature* **620**, 1117–1125 (2023).
- A. H. Lewis, J. Grandl, Piezo1 ion channels inherently function as independent mechanotransducers. *eLife* **10**, e70988 (2021).
- R. Syeda, M. N. Florendo, C. D. Cox, J. M. Kefauver, J. S. Santos, B. Martinac, A. Patapoutian, Piezo1 channels are inherently mechanosensitive. *Cell Rep.* **17**, 1739–1746 (2016).
- X. Chen, S. Wanggou, A. Bodalia, M. Zhu, W. Dong, J. J. Fan, W. C. Yin, H.-K. Min, M. Hu, D. Draghici, W. Dou, F. Li, F. J. Coutinho, H. Whetstone, M. M. Kushida, P. B. Dirks, Y. Song, C. Hui, Y. Sun, L.-Y. Wang, X. Li, X. Huang, A feedforward mechanism mediated by mechanosensitive ion channel PIEZO1 and tissue mechanics promotes glioma aggression. *Neuron* **100**, 799–815.e7 (2018).
- P. Ridone, E. Pandzic, M. Vassalli, C. D. Cox, A. Macmillan, P. A. Gottlieb, B. Martinac, Disruption of membrane cholesterol organization impairs the activity of PIEZO1 channel clusters. *J. Gen. Physiol.* **152**, e201912515 (2020).
- M. Yao, A. Tijore, D. Cheng, J. V. Li, A. Hariharan, B. Martinac, G. Tran Van Nhieu, C. D. Cox, M. Sheetz, Force- and cell state-dependent recruitment of Piezo1 drives focal adhesion dynamics and calcium entry. *Sci. Adv.* **8**, eabo1461 (2022).
- J. Hu, Q. Chen, H. Zhu, L. Hou, W. Liu, Q. Yang, H. Shen, G. Chai, B. Zhang, S. Chen, Z. Cai, C. Wu, F. Hong, H. Li, S. Chen, N. Xiao, Z. Wang, X. Zhang, B. Wang, L. Zhang, W. Mo, Microglial Piezo1 senses A β fibril stiffness to restrict Alzheimer's disease. *Neuron* **111**, 15–29.e8 (2023).
- K. L. Ellefsen, L. R. Holt, A. C. Chang, J. L. Nourse, J. Arulmoli, A. H. Mekhdjian, H. Abuwarda, F. Tombola, L. A. Flanagan, A. R. Dunn, I. Parker, M. M. Pathak, Myosin-II mediated traction forces evoke localized Piezo1-dependent Ca²⁺ flickers. *Commun. Biol.* **2**, 1–13 (2019).
- S. M. Shin, B. Itson-Zoske, F. Fan, U. Gani, M. Rahman, Q. H. Hogan, H. Yu, Peripheral sensory neurons and non-neuronal cells express functional Piezo1 channels. *Mol. Pain* **19**, 17448069231174315 (2023).
- Z.-Y. Yu, H. Gong, S. Kesteven, Y. Guo, J. Wu, J. V. Li, D. Cheng, Z. Zhou, S. E. Iismaa, X. Kaidonis, R. M. Graham, C. D. Cox, M. P. Feneley, B. Martinac, Piezo1 is the cardiac

- mechanosensor that initiates the cardiomyocyte hypertrophic response to pressure overload in adult mice. *Nat. Cardiovasc. Res.* **1**, 577–591 (2022).
33. J. R. Holt, W.-Z. Zeng, E. L. Evans, S.-H. Woo, S. Ma, H. Abuwarda, M. Loud, A. Patapoutian, M. M. Pathak, Spatiotemporal dynamics of PIEZO1 localization controls keratinocyte migration during wound healing. *eLife* **10**, e65415 (2021).
 34. G. A. Bertaccini, I. Casanellas, E. L. Evans, J. L. Nourse, G. D. Dickinson, G. Liu, S. Seal, A. T. Ly, J. R. Holt, T. D. Wijerathne, S. Yan, E. E. Hui, J. J. Lacroix, M. M. Panicker, S. Upadhyayula, I. Parker, M. M. Pathak, Visualizing PIEZO1 localization and activity in hiPSC-derived single cells and organoids with HaloTag technology. *bioRxiv* [Preprint] (2024). <https://doi.org/10.1101/2023.12.22.573117>.
 35. Z. Zhou, X. Ma, Y. Lin, D. Cheng, N. Bavi, G. A. Secker, J. V. Li, V. Janbandhu, D. L. Sutton, H. S. Scott, M. Yao, R. P. Harvey, N. L. Harvey, B. Corry, Y. Zhang, C. D. Cox, MyoD-family inhibitor proteins act as auxiliary subunits of Piezo channels. *Science* **381**, 799–804 (2023).
 36. G. Vaisey, P. Banerjee, A. J. North, C. A. Haselwandter, R. MacKinnon, Piezo1 as a force-through-membrane sensor in red blood cells. *eLife* **11**, e82621 (2022).
 37. A. C. Dumitru, A. Stommen, M. Koehler, A.-S. Cloos, J. Yang, A. Leclercqz, D. Tyteca, D. Alsteens, Probing PIEZO1 localization upon activation using high-resolution atomic force and confocal microscopy. *Nano Lett.* **21**, 4950–4958 (2021).
 38. S. Yaganoglu, K. Kalyviotis, C. Vagena-Pantoula, D. Jülich, B. M. Gaub, M. Welling, T. Lopes, D. Lachowski, S. S. Tang, A. Del Rio Hernandez, V. Salem, D. J. Müller, S. A. Holley, J. Vermot, J. Shi, N. Helassa, K. Török, P. Pantazis, Highly specific and non-invasive imaging of Piezo1-dependent activity across scales using GenEPI. *Nat. Commun.* **14**, 4352 (2023).
 39. W. Jiang, J. S. Del Rosario, W. Botello-Smith, S. Zhao, Y. Lin, H. Zhang, J. Lacroix, T. Rohacs, Y. L. Luo, Crowding-induced opening of the mechanosensitive Piezo1 channel in silico. *Commun. Biol.* **4**, 84 (2021).
 40. F. Balzarotti, Y. Eilers, K. C. Gwosch, A. H. Gynnå, V. Westphal, F. D. Stefani, J. Elf, S. W. Hell, Nanometer resolution imaging and tracking of fluorescent molecules with minimal photon fluxes. *Science* **355**, 606–612 (2017).
 41. K. C. Gwosch, J. K. Pape, F. Balzarotti, P. Hoess, J. Ellenberg, J. Ries, S. W. Hell, MINFLUX nanoscopy delivers 3D multicolor nanometer resolution in cells. *Nat. Methods* **17**, 217–224 (2020).
 42. L. M. Ostersehl, D. C. Jans, A. Wittek, J. Keller-Findeisen, K. Inamdar, S. J. Sahl, S. W. Hell, S. Jakobs, DNA-PAINT MINFLUX nanoscopy. *Nat. Methods* **19**, 1072–1075 (2022).
 43. M. Moroni, M. R. Servin-Vences, R. Fleischer, O. Sánchez-Carranza, G. R. Lewin, Voltage gating of mechanosensitive PIEZO channels. *Nat. Commun.* **9**, 1096 (2018).
 44. R. I. Slavchov, T. Nomura, B. Martinac, M. Sokabe, F. Sachs, Gigaseal mechanics: Creep of the gigaseal under the action of pressure, adhesion, and voltage. *J. Phys. Chem. B* **118**, 12660–12672 (2014).
 45. W. M. Botello-Smith, W. Jiang, H. Zhang, A. D. Ozkan, Y.-C. Lin, C. N. Pham, J. J. Lacroix, Y. Luo, A mechanism for the activation of the mechanosensitive Piezo1 channel by the small molecule Yoda1. *Nat. Commun.* **10**, 4503 (2019).
 46. L.-Y. Chiang, K. Poole, B. E. Oliveira, N. Duarte, Y. A. B. Sierra, L. Bruckner-Tuderman, M. Koch, J. Hu, G. R. Lewin, Laminin-332 coordinates mechanotransduction and growth cone bifurcation in sensory neurons. *Nat. Neurosci.* **14**, 993–1000 (2011).
 47. K. Xu, G. Zhong, X. Zhuang, Actin, spectrin, and associated proteins form a periodic cytoskeletal structure in axons. *Science* **339**, 452–456 (2013).
 48. J. He, R. Zhou, Z. Wu, M. A. Carrasco, P. T. Kurshan, J. E. Farley, D. J. Simon, G. Wang, B. Han, J. Hao, E. Heller, M. R. Freeman, K. Shen, T. Maniatis, M. Tessier-Lavigne, X. Zhuang, Prevalent presence of periodic actin-spectrin-based membrane skeleton in a broad range of neuronal cell types and animal species. *Proc. Natl. Acad. Sci. U.S.A.* **113**, 6029–6034 (2016).
 49. T. M. Svitkina, Actin cell cortex: Structure and molecular organization. *Trends Cell Biol.* **30**, 556–565 (2020).
 50. T. Grevesse, B. E. Dabiri, K. K. Parker, S. Gabriele, Opposite rheological properties of neuronal microcompartments predict axonal vulnerability in brain injury. *Sci. Rep.* **5**, 9475 (2015).
 51. M. N. Young, M. J. Sindoni, A. H. Lewis, S. Zauscher, J. Grandl, The energetics of rapid cellular mechanotransduction. *Proc. Natl. Acad. Sci. U.S.A.* **120**, e2215747120 (2023).
 52. K. Poole, R. Herget, L. Lapatsina, H.-D. Ngo, G. R. Lewin, Tuning Piezo ion channels to detect molecular-scale movements relevant for fine touch. *Nat. Commun.* **5**, 3520 (2014).
 53. Y. Qi, L. Andolfi, F. Frattini, F. Mayer, M. Lazzarino, J. Hu, Membrane stiffening by STOML3 facilitates mechanosensation in sensory neurons. *Nat. Commun.* **6**, 8512 (2015).
 54. C. Wetzel, J. Hu, D. Riethmacher, A. Benckendorff, L. Harder, A. Eilers, R. Moshourab, A. Kozlenkov, D. Labuz, O. Caspani, B. Erdmann, H. Machelksa, P. A. Heppenstall, G. R. Lewin, A stomatin-domain protein essential for touch sensation in the mouse. *Nature* **445**, 206–209 (2007).
 55. K. A. Smith, E. Chuntharpursat-Bon, O. V. Povstyan, M. Debant, J. A. Kinsella, C. Revill, C. Fagnen, J. Shi, R. Foster, D. J. Beech, A. C. Kalli, Regulation of PIEZO1 channel force sensitivity by interblade handshaking. *Sci. Adv.* **11**, eadt7046 (2025).
 56. I. Schaefer, C. Verkest, L. Vespermann, T. Mair, H. Voß, N. Zeitzschel, S. G. Lechner, PKA mediates modality-specific modulation of the mechanically gated ion channel PIEZO2. *J. Biol. Chem.* **299**, 104782 (2023).
 57. G. Parsonage, K. Cuthbertson, N. Endesh, N. Murciano, A. J. Hyman, C. H. Revill, O. V. Povstyan, E. Chuntharpursat-Bon, M. Debant, M. J. Ludlow, T. S. Futers, L. Lichtenstein, J. A. Kinsella, F. Bartoli, M. G. Rotordam, N. Becker, A. Brüggemann, R. Foster, D. J. Beech, Improved PIEZO1 agonism through 4-benzoic acid modification of Yoda1. *Br. J. Pharmacol.* **180**, 2039–2063 (2023).
 58. A. H. Lewis, M. E. Cronin, J. Grandl, Piezo1 ion channels are capable of conformational signaling. *Neuron* **112**, 3161–3175.e5 (2024).
 59. S. Yang, X. Miao, S. Arnold, B. Li, A. T. Ly, H. Wang, M. Wang, X. Guo, M. M. Pathak, W. Zhao, C. D. Cox, Z. Shi, Membrane curvature governs the distribution of Piezo1 in live cells. *Nat. Commun.* **13**, 7467 (2022).
 60. R. G. Parton, K.-A. McMahon, Y. Wu, Caveolae: Formation, dynamics, and function. *Curr. Opin. Cell Biol.* **65**, 8–16 (2020).
 61. C. G. Hansen, B. J. Nichols, Exploring the caves: Cavins, caveolins and caveolae. *Trends Cell Biol.* **20**, 177–186 (2010).
 62. L. Cui, H. Li, Y. Xi, Q. Hu, H. Liu, J. Fan, Y. Xiang, X. Zhang, W. Shui, Y. Lai, Vesicle trafficking and vesicle fusion: Mechanisms, biological functions, and their implications for potential disease therapy. *Mol. Biomed.* **3**, 29 (2022).
 63. S. C. Harrison, T. Kirchhausen, Conservation in vesicle coats. *Nature* **466**, 1048–1049 (2010).
 64. S. G. Brohawn, N. C. Leksa, E. D. Spear, K. R. Rajashankar, T. U. Schwartz, Structural evidence for common ancestry of the nuclear pore complex and vesicle coats. *Science* **322**, 1369–1373 (2008).
 65. H. Mazal, A. Schambony, V. Sandoghdar, Cryogenic light microscopy with Ångstrom precision deciphers structural conformations of PIEZO1. *bioRxiv* [Preprint] (2024). <https://doi.org/10.1101/2024.12.22.629944>.
 66. B. M. Gaub, K. C. Kasuba, E. Mace, T. Strittmatter, P. R. Laskowski, S. A. Geissler, A. Hierlemann, M. Fussenegger, B. Roska, D. J. Müller, Neurons differentiate magnitude and location of mechanical stimuli. *Proc. Natl. Acad. Sci. U.S.A.* **117**, 848–856 (2020).
 67. E. M. Kugler, K. Michel, F. Zeller, I. E. Demir, G. O. Ceyhan, M. Schemann, G. Mazzuoli-Weber, Mechanical stress activates neurites and somata of myenteric neurons. *Front. Cell. Neurosci.* **9**, 342 (2015).
 68. Z. Shi, Z. T. Graber, T. Baumgart, H. A. Stone, A. E. Cohen, Cell membranes resist flow. *Cell* **175**, 1769–1779.e13 (2018).
 69. Z. Shi, S. Innes-Gold, A. E. Cohen, Membrane tension propagation couples axon growth and collateral branching. *Sci. Adv.* **8**, eabo1297 (2022).
 70. W. Jiang, T. D. Wijerathne, H. Zhang, Y.-C. Lin, S. Jo, W. Im, J. J. Lacroix, Y. L. Luo, Structural and thermodynamic framework for PIEZO1 modulation by small molecules. *Proc. Natl. Acad. Sci. U.S.A.* **120**, e2310933120 (2023).
 71. C. Verkest, L. Roettger, N. Zeitzschel, S. G. Lechner, 3D-MINFLUX nanoscopy reveals distinct allosteric mechanisms for activation and modulation of PIEZO1 by Yoda1. *bioRxiv* [Preprint] (2025). <https://doi.org/10.1101/2025.07.10.664100>.
 72. A. H. Lewis, J. Grandl, Mechanical sensitivity of Piezo1 ion channels can be tuned by cellular membrane tension. *eLife* **4**, e12088 (2015).
 73. B. C. Campbell, E. M. Nabel, M. H. Murdock, C. Lao-Peregrin, P. Tsoulfas, M. G. Blackmore, F. S. Lee, C. Liston, H. Morishita, G. A. Petsko, mGreenLantern: A bright monomeric fluorescent protein with rapid expression and cell filling properties for neuronal imaging. *Proc. Natl. Acad. Sci. U.S.A.* **117**, 30710–30721 (2020).
 74. H. Götzke, M. Kilisch, M. Martínez-Carranza, S. Sograte-Idrissi, A. Rajavel, T. Schlichthaerle, N. Engels, R. Jungmann, P. Stenmark, F. Opazo, S. Frey, The ALFA-tag is a highly versatile tool for nanobody-based bioscience applications. *Nat. Commun.* **10**, 4403 (2019).
 75. F. J. Taberner, V. Prato, I. Schaefer, K. Schrenk-Siemens, P. A. Heppenstall, S. G. Lechner, Structure-guided examination of the mechanogating mechanism of PIEZO2. *Proc. Natl. Acad. Sci. U.S.A.* **116**, 14260–14269 (2019).
 76. Y. Zhang, M. Rózsa, Y. Liang, D. Bushey, Z. Wei, J. Zheng, D. Reep, G. J. Broussard, A. Tsang, G. Tsegaye, S. Narayan, C. J. Obara, J.-X. Lim, R. Patel, R. Zhang, M. B. Ahrens, G. C. Turner, S.-H. Wang, W. L. Korff, E. R. Schreiter, K. Svoboda, J. P. Hasseman, I. Kolb, L. L. Looger, Fast and sensitive GCaMP calcium indicators for imaging neural populations. *Nature* **615**, 884–891 (2023).
 77. F. A. Ran, P. D. Hsu, C.-Y. Lin, J. S. Gootenberg, S. Konermann, A. E. Trevino, D. A. Scott, A. Inoue, S. Matoba, Y. Zhang, F. Zhang, Double nicking by RNA-guided CRISPR Cas9 for enhanced genome editing specificity. *Cell* **154**, 1380–1389 (2013).
 78. O. Sánchez-Carranza, S. Chakrabarti, J. Kühnemund, F. Schwaller, V. Bégay, J. A. García-Contreras, L. Wang, G. R. Lewin, Piezo2 voltage-block regulates mechanical pain sensitivity. *Brain* **147**, 3487–3500 (2024).
 79. K. Miura, Bleach correction ImageJ plugin for compensating the photobleaching of time-lapse sequences. F1000Research 9:1494 [Preprint] (2020). <https://doi.org/10.12688/f1000research.27171.1>.
 80. D. Ershov, M.-S. Phan, J. W. Pylvänäinen, S. U. Rigaud, L. Le Blanc, A. Charles-Orszag, J. R. W. Conway, R. F. Laine, N. H. Roy, D. Bonazzi, G. Duménil, G. Jacquemet, J.-Y. Tinevez, TrackMate 7: Integrating state-of-the-art segmentation algorithms into tracking pipelines. *Nat. Methods* **19**, 829–832 (2022).

81. J.-Y. Tinevez, N. Perry, J. Schindelin, G. M. Hoopes, G. D. Reynolds, E. Laplantine, S. Y. Bednarek, S. L. Shorte, K. W. Eliceiri, TrackMate: An open and extensible platform for single-particle tracking. *Methods* **115**, 80–90 (2017).
82. S. J. Sahl, J. Matthias, K. Inamdar, M. Weber, T. A. Khan, C. Brüser, S. Jakobs, S. Becker, C. Griesinger, J. Broichhagen, S. W. Hell, Direct optical measurement of intramolecular distances with angstrom precision. *Science* **386**, 180–187 (2024).
83. P. T. Boggs, J. R. Donaldson, R. h. Byrd, R. B. Schnabel, Algorithm 676: ODRPACK: Software for weighted orthogonal distance regression. *ACM Trans. Math. Softw.* **15**, 348–364 (1989).

Acknowledgments: We thank A. Failla and the team of the imaging core facility at UKE Hamburg (DFG Research Infrastructure Portal #RI_00489) for technical assistance with the MINFLUX microscope. Funding for the MINFLUX microscope was awarded by the Hamburgische Investitions- und Förderbank (IFB, grant no. 51164232) under the Operational Programme Hamburg ERDF 2014-2020, REACT-EU of the European Regional Development Fund (ERDF). We also thank H. Al-Marsoomi and C. Lüchau for assistance with cloning and cell culture. **Funding:** This work was funded by the ERC Pain Channels (101142488) to G.R.L. and DFG research grant LE3210/3-3 (S.G.L.). **Author contributions:** C.V.: Investigation, writing—review and editing,

methodology, data curation, validation, formal analysis, software, and visualization. L.R.: Investigation. N.Z.: Investigation. J.H.: Investigation and formal analysis. O.S.-C.: Investigation and formal analysis. A.T.-L.H.: Investigation and formal analysis. G.R.L.: Funding acquisition, methodology, supervision, and resources. S.G.L.: Writing—original draft, conceptualization, investigation, writing—review and editing, methodology, resources, funding acquisition, data curation, validation, supervision, formal analysis, software, project administration, and visualization. **Competing interests:** The authors declare that they have no competing interests. **Data and materials availability:** All data supporting the article, such as the MINFLUX and patch-clamp analysis outputs for each experimental condition, as well as Matlab codes for MINFLUX data analysis and reproduction of figures are available at <https://doi.org/10.5281/zenodo.16789916>. N2a-Stoml3^{-/-} cells were created by G.R.L. and colleagues and are provided upon request. All data needed to evaluate the conclusions in the paper are present in the paper and/or the Supplementary Materials.

Submitted 13 May 2025

Accepted 24 September 2025

Published 22 October 2025

10.1126/sciadv.ady8052